Construction of Position Sensitive Avalanche Counters

M.B. Tsang, W.G. Lynch, Z.R. Xu, G. Poggi and G.K. Gelbke

Position sensitive avalanche detectors (PSAD) have now become widely used in heavy ion experiments when good timing resolution is needed in conjunction with large solid angles and high counting rates. In these detectors a sense wire plane is placed midway between cathode and anode of the avalanche detector. Both the cathode and the anode are made out of thin aluminized mylar or polypropylene. Position along the sense wire plane is determined via a delay line read out. Two designs of PSAD detectors similar to the design of Harrach and Specht[1] have been constructed at NSCL. They share the following common characteristics:

gap between electrodes	3 mm
distance between adjacent wires	2 mm
position read out	tapped delay line
delay per tap	2 ns
pressure range	4-20 torr
filling gas	hexane, isobutane
operating voltage	500-800 volts
expected position resolution	1 mm

The designs of the two PSAD's currently under construction differ primarily in that the larger PSAD (with an active area 20 cm x 16 cm) relies on gaseous diffusion to replenish the ionizing gas in the active volume of the detector while the smaller PSAD (12 cm x 12 cm active area) has internal gas tubing which forces the gas flow through each segment of the detector.

We are constructing two of the larger PSAD's. One of these two detectors has been tested at 5 and 10 torr with ^{241}Am and ^{252}Cf sources. This detector can hold in excess of 500 volts at 5 torr and in excess of 600 volts at 10 torr indicating that gaseous diffusion should be sufficient to replenish the ionizing gas. These voltages and pressure are more than sufficient for the detector of fission fragments and heavy ions.

We have also constructed a third PSAD of the smaller design. To obtain addition energy loss information, a 3 cm long proportional counter has been inserted midway between the avalanche segment containing the y senser wire plane (y detector) and the avalanche segment containing the x senser wire plane (x detector). This PSAD has been tested at 5, 10 and 15 torr of isobutane

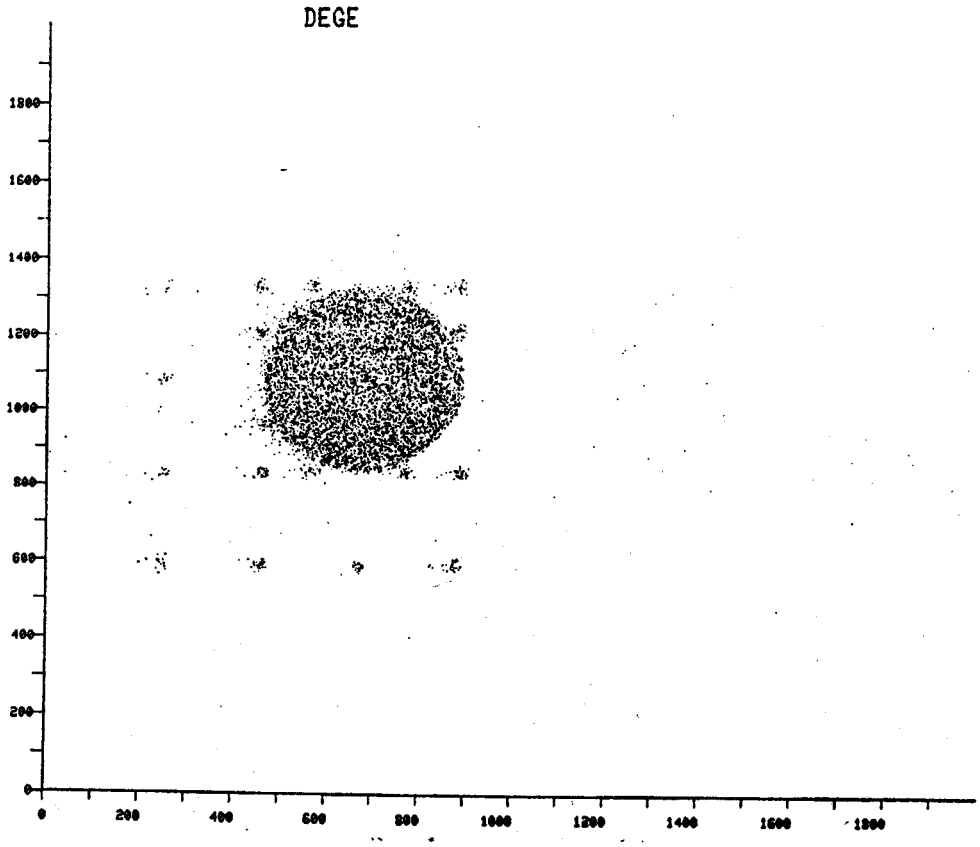

Fig. 1. Computer generated position image of x vs. y for the mask shown in Fig. 2.

with ^{241}Am and ^{252}Cf sources. Each of the avalanche segments holds in excess of 500 V at 5 torr; 700 V at 10 torr and 800 V at 15 torr while the proportional counter holds in excess of 700 V at 10 torr and 1400 V at 15 torr. This PSAD has also been used in transmission geometry with 2.5×10^{-4} cm thick entrance and exit windows and backed by a 20 cm^2 Si surface barrier detector in the experiment measuring charged particles emitted in the reaction of 300 MeV $^{40}Ca + ^{40}Ca$. Preliminary data indicate an intrinsic time resolution better than 300 ps for each avalanche segment. A plot of ΔE measured in the gas proportional counter vs E measured in the Si stop detector shows separation between various charge groups. However, insufficient statistics prevented quantitative measurement of the charge resolution. A two dimensional plot of the x-y position spectrum is shown in Fig. 1. This is an image of the mask shown in Fig. 2. The small holes are 2.38 mm in diameter.

At present we are using anode and cathode foils consisting of commercially made aluminized mylar 2×10^{-4} cm thick. These foils are too thick for measurement of fission fragment correlations. We are planning to construct suitable foils by evaporating a conducting layer on stretched polypropylene which can be made as thin as 4×10^{-5} cm in thickness.

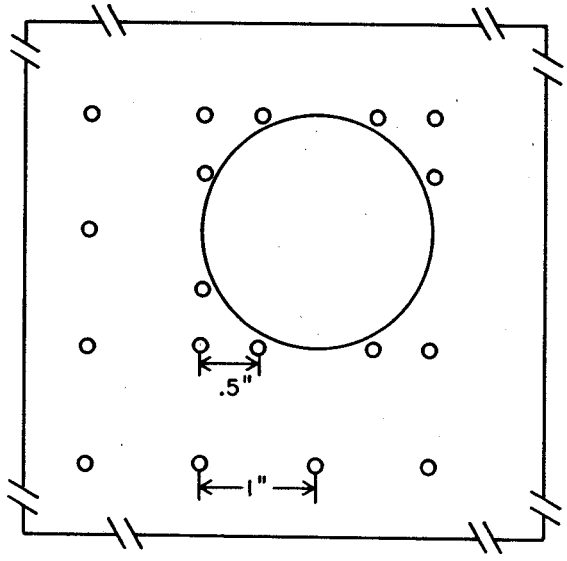

Fig. 2. Schematic diagram of the mask used. The big hole in the center is 5.08 cm in diameter. All the small holes are 2.38 mm in diameter.

1. Harrah and Specht , NIM 164 (1979) 477.

Construction of a Multiwire Proportional Chamber

R. Tickle,[+] G. Crawley, W.G. Lynch, M.B. Tsang and J. Yurkon

Since its invention by Charpak more than a decade ago, the multiwire proportional chamber (MWPC) has developed into one of the most versatile and widely used detectors in high energy physics. Although to date MWPC have found little application in nuclear physics laboratories, this may change after the newer heavy-ion accelerators are operational and complex experiments using considerably higher energies and a wide variety of heavy-ion projectiles become more commonplace.

Because the MWPC provides a detection system with a large solid angle and high count rate capability for a relatively modest expense, we have designed a prototype chamber to be used in studies of light-ion emission in heavy-ion induced reactions at projectile energies >10 MeV per nucleon. In addition to the two anode planes required for X and Y position information, the chamber will contian a third anode plane to resolve the position ambiguity which arises when several ions traverse the chamber simultaneously.

Some of the principal features of the detector are:

sensitive area: 15.5 cm x 15.5 cm
anode-cathode spacing: 6 mm
wire spacing: 2.54 mm
pressure range: 0.5 - 1.0 atm
filling gas: methane, isobutane
operating voltage: 3300 - 3800 volts.

To reduce the mg/cm^2 thickness of the detector, some of the cathodes are common to two anodes. The design consists of three contiguous cells having a total of four cathode planes (aluminized mylar) and three anodes. The anode wires will be paired electrically which will result in a position resolution of approximately 5 mm (0.8° with a target-detector distance of 35 cm). The readout system will have an amplifier-discriminator (LeCroy PCOS lll) for each pair of wires.

+ University of Michigan, Ann Arbor, MI

A Position Sensitive Proportional Counter for a Tritium Beta Decay Experiment

John Yurkon and Hamish Robertson

A prototype position sensitive proportional counter of cylindrical geometry was constructed. It has an active volume of 0.95 cm^3, and an entrance window of .83 mg/cm^3 aluminized mylar. Details are shown in Fig. 1. Center wires of carbon coated quartz, of various dimensions, and carbon graphite filaments were used. Various gas fills and pressures were tried. To test the counter several sources were used. A Fe^{55} x-ray source, and a well collimated electron gun capable of producing 40 KeV electrons. A collimated Th C' source was also used to establish the position scale.

The electronics consisted of a two Ortec 109 A preamplifiers, two Ortec 451 spectroscopy amplifiers. A Canberra 1463A Sum-amplifier, and an analog divider. The analog divider is a Phil Marchant design.

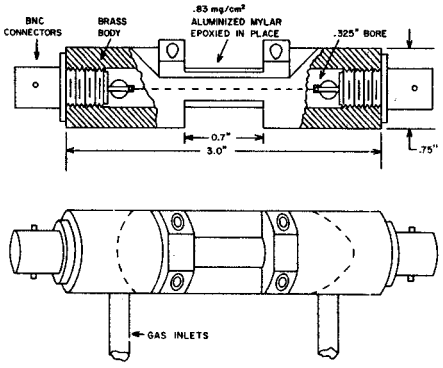

Fig. 1. Details of proportional counter.

The performance of the counter can be seen in the following figures: with a gas fill of 980 torr of isobutane, center wire of 1 mil quartz, and bias of 1700 volts, a collimated Th C' surface was moved along the counter. The results are shown in Fig. 2. The peaks are .76 cm apart, and 1.4 mm FWHM. The bias was raised to 2500 volts and a Fe^{55} energy spectra accumulated. This is shown in Fig. 3.

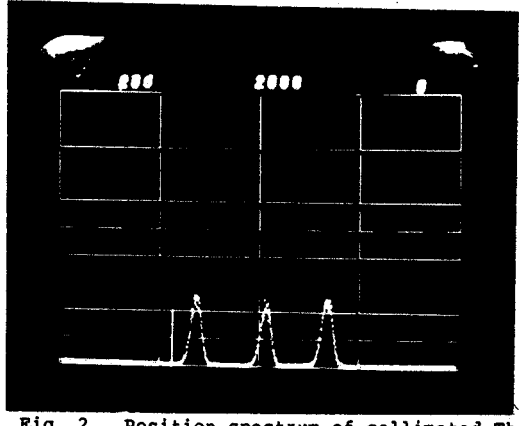

Fig. 2. Position spectrum of collimated Th C' source.

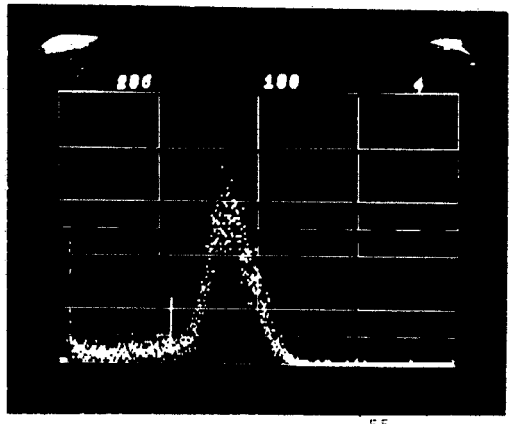

Fig. 3. Energy spectrum of Fe^{55}.

The response to 40 KeV electrons is shown in figures 4 and 5. The detector was operated at approximately 1500 torr of isobutane with 2700 bias. The energy spectra is shown in Fig. 4. It has a 20% energy resolution. The position resolution is shown in Fig. 5. It has a resolution of 2.7 mm.

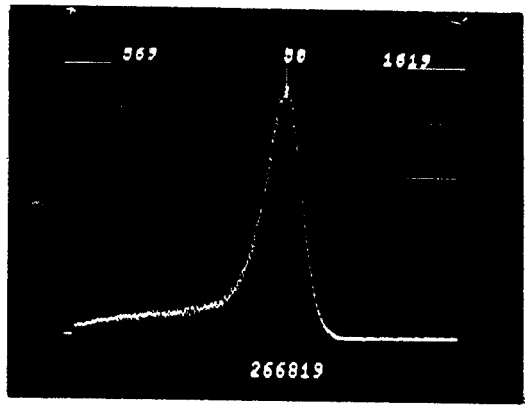

Fig. 4. Energy response to 40 keV electrons.

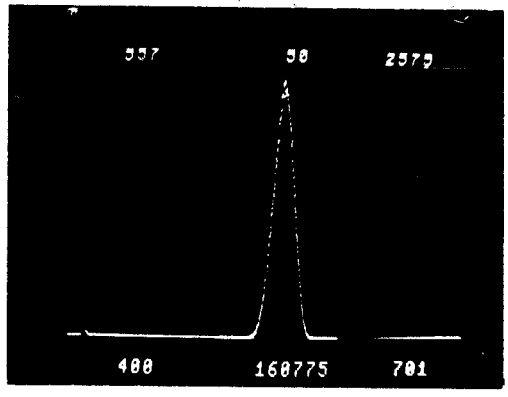

Fig. 5. Position spectrum of collimated 40 keV electrons.

The Pulse-Height Correction Method for Improving Ge γ-ray Detectors

N. Matsushita, J. Kasagi and Wm. C. McHarris

The pulse-height correction method for improving both the energy resolution and the peak-to-Compton ratios from Ge γ-ray detectors, in particular those that have been damaged by neutrons, works basically as follows: By discriminating among the rise-times (in the nsec range) of the pulses from a Ge or Ge(Li) detector, one can select only those pulses (normally having the fastest rise-times) that correspond to the best, or undamaged, portions of the detector. Thus, the detector output can be improved immediately, albeit at the expense of decreased efficiency. However, we discovered[1] that there is a regular correlation between the pulse rise-times and the completeness of charge collection in a detector - hence, in the shift in position of a photopeak. Thus, by adding a pulse-height correction to compensate for the effects of varying rise-time, an improved composite spectrum can be obtained without significant loss in detector efficiency.

Our original method,[1] using a linear correlation between the rise-time and the energy shift, works quite well for planar detectors. For detectors with more complex geometries, e.g., coaxial detectors, it does not work so well. In Fig. 1

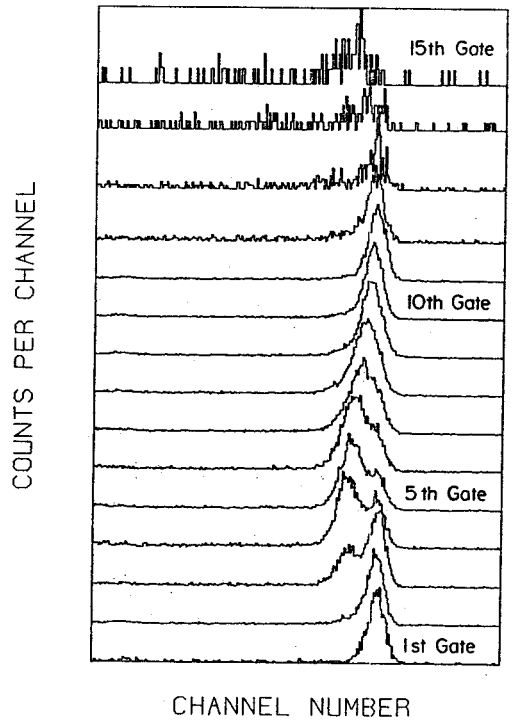

Fig. 1. Correlation between position/shape of the photopeak vs rise-time for the ^{60}Co 1332.513-keV γ ray. Taken with a ≈16% efficient true coaxial analysis. The fastest rise-times are included in Gate 1, with slower and slower rise-times in increasing gate numbers, until the slowest rise-times are reached in Gate 15.

we show the correlation between the rise-time and the position/shape of the ^{60}Co 1332.513-keV photopeak taken by our original method, using a medium size (≈16% efficient) true coaxial Ge(Li) detector. The lowest numbered gates compound to the fastest rise-times, and vice versa. With increasing rise-times, not only does the peak become broader and shift downward in energy, but also, it actually splits into a doublet. Since the lower-energy component of such a doublet also exhibits the low-energy tailing expected from incomplete charge collection from, say, neutron-damaged portions of the detector, it is reasonable to assume that this lower-energy component results from such neutron-damaged portions.

For a planar detector the above analysis would be essentially complete, but for a coaxial detector there is a basic difference in the pulse-shape formation: This depends on the electric field as a function of position inside the detector's sensitive region--this in addition to any traps present in damaged or poor-quality regions. Thus, a simple two parameter analysis is insufficient for analyzing the spectrum and synthesizing an improved spectrum. One must make a more detailed analysis of the pulse shape itself. We have found that analyzing the rise-time in two increments, i.e., between points A and B and between A and C, gives adequate results. With this procedure we have been able to improve the energy resolution of the above detector by some 43%.

In Fig. 2 we show a block diagram of the electronics for such a triple-correlation experiment. Here we analyzed the correlation between the 0.1-0.5 and the 0.1-0.7 fraction of the rise-time (using a constant-fraction timing discriminator). Figure 3 shows the expected correlations. If there were no trapping or geometric effects from a varying electric field, the correlation between the two fractions should be linear, and we would expect the solid line. However, trapping and geometric effects will wash out this relation, resulting in an area correlation such as that between the dashed lines. (This is easiest to visualize in the case of trapping, where trapping can occur at varying places during the course of change collection.)

In Fig. 4 we show an experimental three-parameter correlation among the centroid of the ^{60}Co 1332.513-keV photopeak and the two TAC signals. After an <u>area</u> event-by-event correction, the energy resolution was improved by 43%. The raw and corrected spectra are shown in Fig. 5.

Just as the use of more and narrower rise-time slices in our original method would produce better and better synthesized spectra, until diminishing returns set in, so can the use of smaller

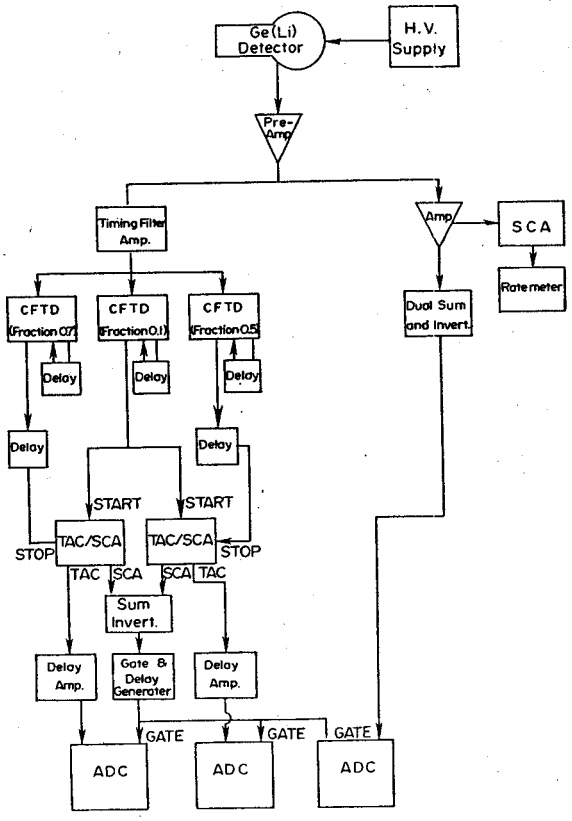

Fig. 2. Block diagram of the electronics for a three-parameter pulse-height correction experiment.

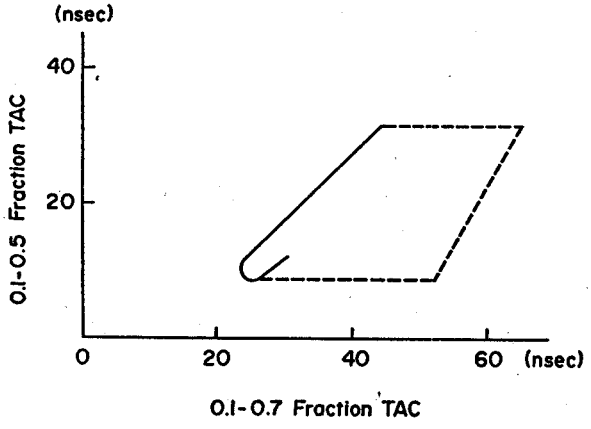

Fig. 3. Expected correlations between the 0.1-0.5-fraction TAC output and the 0.1-0.7-fraction TAC output.

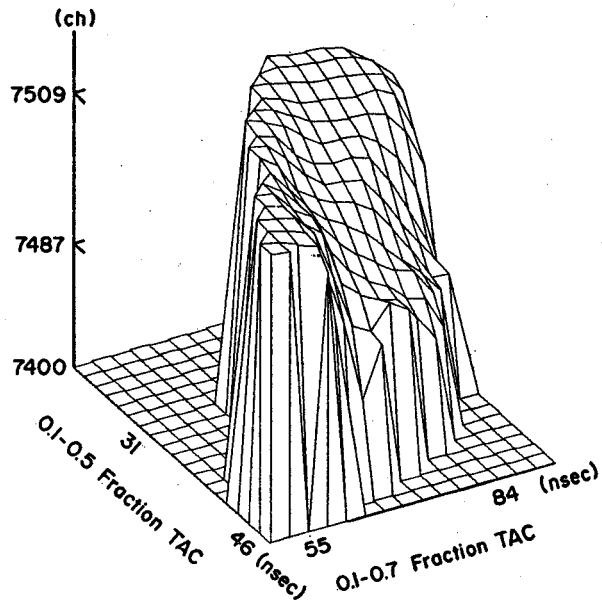

Fig. 4. An experimental correlation between the ^{60}Co 1332.513-keV photopeak and the two rise-time fractional increments. Taken with a ≈16% true coaxial Ge(Li) detector, using the electronics of Fig. 2.

and smaller rise-time correlation areas result in similarly improved spectra with our extended procedure. In addition, adding more constant-fraction timing discriminators set at different rise-time fractions should allow a nicer analysis of the pulse shape and, consequently, an improved synthesized spectrum - again, until diminishing returns due to the cumbersomeness of the electronics. (Also, the use of ORTEC model-552 pulse-shape analyzers would combine many of the boxes in Fig. 2, resulting in some external simplification of the block diagram.)

As the quality of Ge γ-ray detectors improves yearly, it becomes a moot question as to which is more sensible--electronic methods for improving detectors on hand or trading them in for new detectors. As usual, the best answer is probably a compromise between the two. Our pulse-height correction method makes use of electronics readily available in most nuclear science laboratories (and applied nuclear labs, such as reactor labs), and it can certainly result in significant improvement in existing detectors "until we have funds to buy that better detector". Also, the improvement is most significant for neutron-damaged detectors, and as long as neutron damage to detectors is a fact of life in our laboratories, it should remain a viable technique.

A paper on the pulse-height correction method with considerably more detail had been submitted to Nuclear Instruments and Methods.[2]

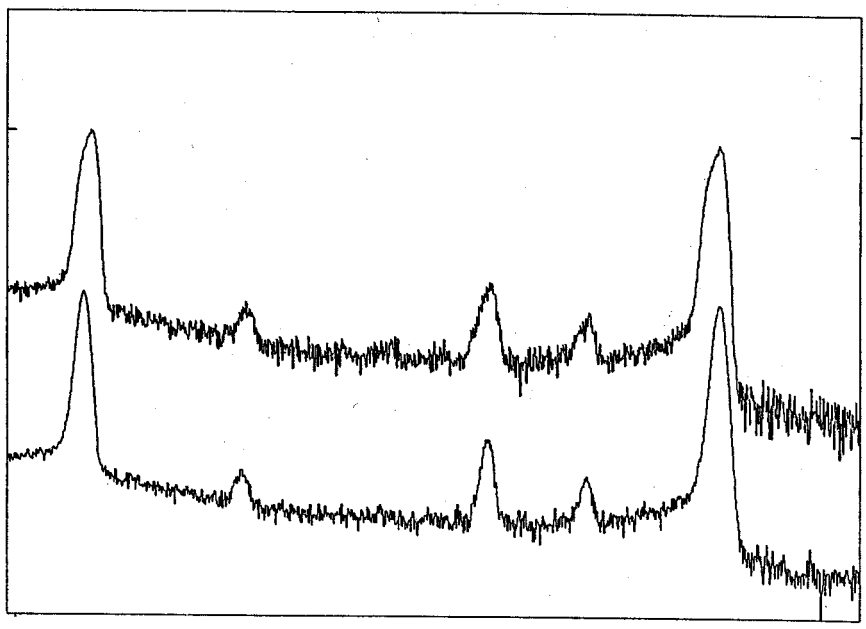

Fig. 5. Comparison between raw and systhesized spectra for the ^{60}Co 1332.513 keV γ ray. Same data as in Fig. 4. The synthisized spectrum resulted from a three-parameter pulse-height correction procedure. In it the photopeak resolution is improved by 43% over the raw spectrum.

1. N. Matsushita, Wm. C. McHarris, R.B. Firestone, J. Kasagi and W.H. Kelly, Nucl. Instr. Meth. 179, 119 (1981).

2. N. Matsushita, J. Kasagi and Wm. C. McHarris, submitted to Nucl. Instr. Meth., 1981.

Progress on the Construction of the S320 Spectrograph

R. Blue, S. Bricker, J. Nolen and D. Wickham

The design parameters and overall description of the k=320 spectrograph (S320) were given in last year's annual report. The S320 mechanical layout is shown in the figure. During the past year substantial progress has been made in the construction of this spectrograph. The quadrupole doublet and the dipole have been mounted on a carriage which was constructed in-house. A rail and wheel system has been designed and constructed. The drive (to change scattering angles) will be via a sprocket and chain system which is designed but not installed to date. The sextupole magnet has been designed, constructed, and tested in-house. These are described under separate headings in this annual report. Modifications of the vacuum manifold of the dipole magnet are in progress. Two commercial cryopumps, one for the scattering chamber and one for the magnets, have been purchased and are in-house but not yet installed. The Minnesota scattering chamber has also been received but not installed. Adapter pieces to change the pole tip entrance curvature on the dipole have been designed and are currently being machined by an outside shop. It is now estimated that the S320 will be operational by mid-1982.

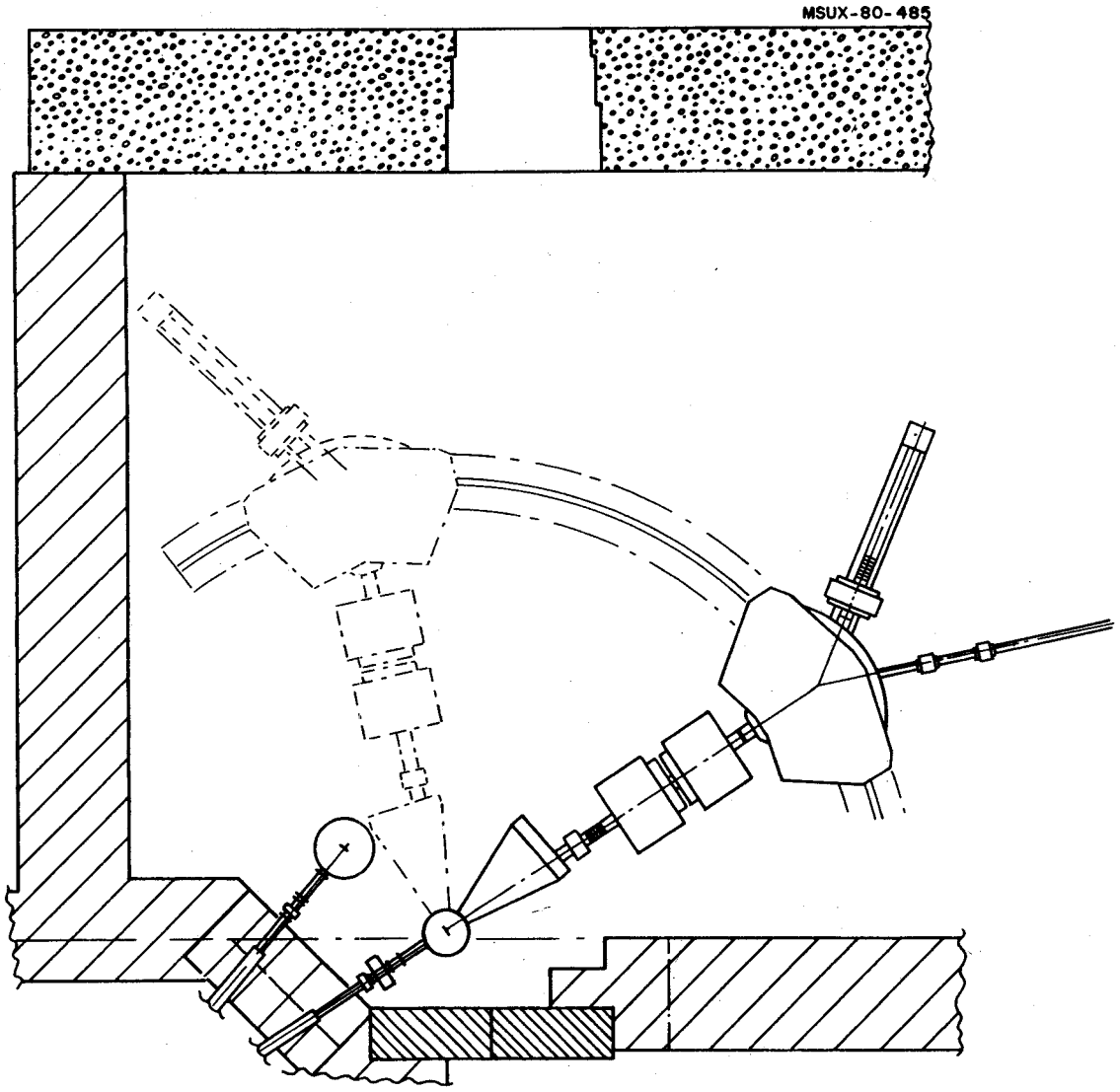

Fig. 1. Plan view of the S320 as it is being assembled in the North vault. It is a QQDS spectrograph and also serves as a switching magnet to direct beam to the Split-pole spectrograph.

S320 Sextupole Design

L.H. Harwood and J.A. Nolen

The optical design for the S320 spectrograph called for a sextupole with a 15 cm diameter aperture. No such magnet was available in this laboratory and none of appropriate overall dimensions were available as surplus equipment from other laboratories. It was therefore decided that one would be designed and built locally. To minimize the overall effort required it was further decided to use a scaled up version of the 10 cm sextupole which was part of the K50 cyclotron beam analysis system.

The first step in producing the new sextupole was to scale up the drawings from the 10 cm unit. After this was done, two-dimensional field calculations were done with the POISSON computer program.[1] The initial calculations were rather slow because of the large gradients involved in the sextupole field. However, POISSON has a feature which permits a problem to be calculated after doing a conformal mapping of the form $w = z^n$ where $w = x' + iky'$, $z = x + iy$, and n is an integer. If a sextupole field is mapped using $n = 3$, then the mapped field will be that of a dipole. The calculations of the "dipole" field converged more quickly than the sextupole field. Figure 1 shows the original and mapped versions of the initial pole tip shape. Notice that the corners in the original geometry are enhanced by the mapping and become cusps in the mapped geometry. Also notice that the volume that the beam actually occupies maps into a small portion of the mapped gap. Thus, in the mapped geometry, we need a "good" field in only a small portion of the problem.

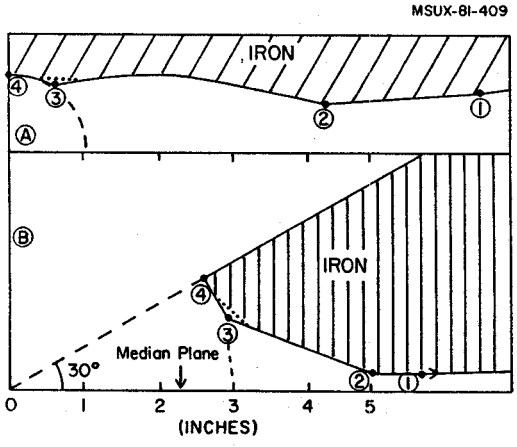

Fig. 1. Illustrations of the unmodified and modified pole-tip shapes for the S320 sextupole. (Note only half of one pole tip is shown. The other half can be obtained by reflection across the dashed line at 30°.) A) shows the conformally mapped geometry and B) shows the actual shape. The circled numbers indicate corresponding points. The dashed circles in A) and B) show the area that the beam can occupy.

Table I gives the multipole expansion coefficients for the mapped field. These non-zero sextupole and decapole components result in a non-uniform field. The field produced when the problem is mapped back to the original geometry had unsatisfactorally large nonsextupole components. Pole tip modifications were needed. The most obvious change was to try to flatten the mapped pole tip by reducing the cusps. The cusp near the center has the most effect on the field in the beam region; therefore we concentrated on it. Keeping in mind that ease of construction was important, one more bevel was added to the unmapped pole tip, as shown in Fig. 1. Several more bevels would have improved the pole tip further (the limit being a flat mapped pole-tip corresponding to a hyperbolic unmapped pole-tip) but would have increased the machining considerably. The multipole coefficients for the new pole shape are listed in Table I. The sextupole and decapole terms have been reduced considerably. The field quality with the new shape was calculated at several field levels and was satisfactory over the range necessary for the S320. The drawings were changed to include the new bevel, and the sextupole was built (see the progress report on the construction and mapping of the sextupole).

Table I. Harmonic Coefficients of the Field[1] of the S320 Sextupole.

N[2]	B_N(initial)	B_N(modified pole)
1	23800	28800
3	2.98	0.445
5	0.376	0.205

1) Calculated field after conformal mapping to to a dipole geometry.

2) $B(R) = \sum_N B_N R^{N-1}$.

1. B.F. Holsinger, private communication.

Construction and Mapping of the Sextupole for the S320 Spectrograph

J. Nolen, M. Distasio, B. Sherrill, N. Kedarnath and M. Pangia

Since last years annual report a sextupole for the S320 was designed, the steel machined by an outside shop, the coils wound in-house using an existing winding fixture, and the current and water connections made (see the separate report on the sextupole design). The 1/4 inch copper conductor was insulated with a slide-on-fiber-glass insulation and was also painted and secured to the yoke with epoxy. The entire winding process took approximately 200 man-hours. The coil has a resistance of 0.12Ω and requires a current of approximately 100 amps, at 12 volts, to reach the 2 kG operating field for the S320. With a cooling water flow rate of about .05 gal/min the sextupole could be run with pole tip fields of at least 4 kG.

Currently, the sextupole is being mapped with the mapping apparatus used to map the K-500 cyclotron field. The apparatus consists of 55 flip coils spaced 1/2 inch apart along a bar. This allows 55 simultaneous measurements, greatly improving the accuracy of the field measurements, while reducing the mapping time. Figure 1 shows the mapping device and the sextupole. The bar containing the flip coils moves horizontally through the magnet measuring the field on the median plane. Fields off the median plane are measured by rotating the magnet.

Fig. 1. Photograph showing the magnet mapping apparatus with the sextupole.

A complete median plane field map, obtained in this way, is shown in Fig. 2. The parameters of interest which can be obtained from such a map are the fringe field coefficients and the effective magnetic length. Table 1 summarizes these parameters and also gives, for comparison, fringe field coefficients measured for the quadrupole doublet used at the entrance of the S320 spectrograph. The coefficients are used in RAYTRACE calculations of the ion-optical properties of the spectrograph.

MSUX-81-434

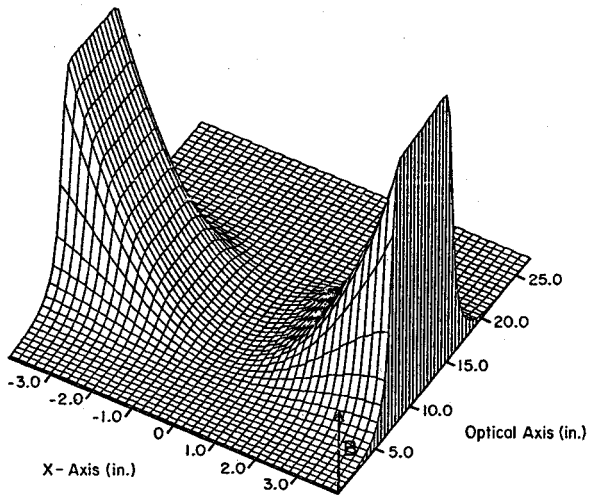

Fig. 2. Two-dimensional median plane magnetic field map. The maximum B-field is 4.4 kG.

Table 1. Measured fringe field coefficients for the sextupole and quadrupole doublet used in the S320 spectrograph. These are the coefficients to be used with the program RAYTRACE. The effective magnetic length of the sextupole and quadrupole are 9.70 in., and 19.46 in. respectively. The corresponding physical lengths are 8.0 in. and 16.0 in.

Coefficient Order	Sextupole	Quadrupole
0	0.239	0.262
1	7.11	5.66
2	-2.80	-2.96
3	-1.82	2.19
4	-	-0.632
5	-	-0.0373

To obtain the fringing field coefficients of the sextupole an iterating procedure was used. For a dipole fringe field the program RAYTRACE uses a function:

$$h(s) = B_z(s)/B_o = 1/(1+\exp(S)), \quad (1)$$

where $S(s) = C_0 + Cs + C_2s^2 + C_3s^3 + C_4s^4 + C_5 s^5$, and s is the distance from the effective edge in units of the dipole gap. For a quadrupole the fringing field, in principle, varies with distance from the quad axis, due to additional gradient terms which appear in (1). However, these new terms are very small and can usually be neglected. Hence the coefficients, C_i, for dipoles and quadrupoles can be obtained by least squares fitting the measured fringe field shapes with equation (1). (These statements are true for these particular quads, but may not be true for all quads.) For a sextupole the additional

gradient terms to be included in (1) are significant and are noticeable as a variation of the fringe field shape with distance from the sextupole axis. We have used an iterative method to include these additional terms in the determination of the coefficients, C_i, for the sextupole as shown in Table 1.

The quality of the sextupole field can be determined by calculating the coefficients of a multipole expansion fitting this field. From this analysis we see the field is almost 97% sextupole at r = 3.0 in., and there are no significant problems with the magnet.

Design of a Non-circular Octupole Magnet for the S320 Spectrograph

B. Sherrill, J. Nolen and L.H. Harwood

Detailed raytracing calculations of the S320 spectrograph show that with an octupole for third-order optical corrections it is possible to obtain a resolution of $\frac{\Delta E}{E} = 10^{-3}$ at $\Omega = 0.5$ msr and an energy range of 20% without substantial "raytracing" with a focal plane detector system. (Without the octupole the solid angle is limited to 0.3 msr.) The primary third order terms in a Taylor's expansion of the image size at the focal plane are (x/θ^3), $(x/\theta^2\delta)$, and $(x/\theta\delta^2)$. Since the first two of these terms produce the major aberrations in the image, they specify the type of remedy. If an octupole is used to correct these terms, (x/θ^3) and $(x/\theta^2\delta)$, its optimum location is between the dipole and sextupole as shown in Fig. 1. At this position the ratio of (x/θ) to (x/δ) has the right magnitude to permit simultaneous correction of both terms.

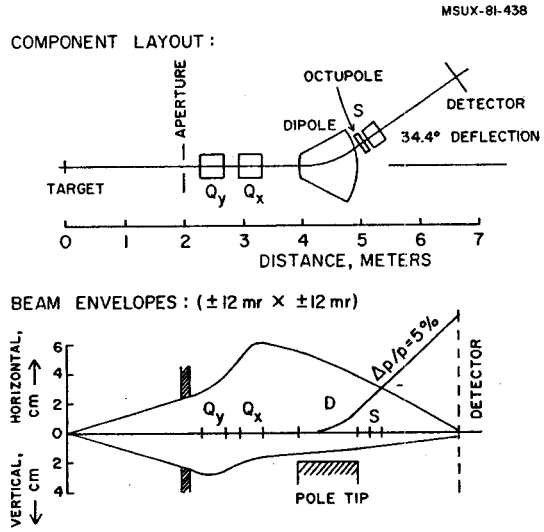

Fig. 1. Diagram of the S320 spectrograph with the proposed octupole.

The constraint placed on an octupole in such a position is that it cannot be over 6 inches in overall height, but must have an effective elliptical aperture with a minor radius of 1.75" and a major radius of 3.5". This constraint precludes the use of a conventional octupole. The solution is to use a current-sheet magnet (H. Ikegami et. al., RCNL Annual Report, (1977) p. 137).

Using Ampere's Law it can be shown

$$\phi_m = - \frac{\partial j}{\partial s}$$

where ϕ_m is the magnetic scaler potential, j is the current density, and s is the arc-length along the interior surface of the magnet. Therefore, with the appropriate distribution of current, j, any desired ϕ_m can be obtained for any shape of iron yoke magnet. A special case of such a magnet is the Panofsky quadrupole (L.N. Hand and W.K. Panofsky, Rev. Sci. Instr., 30 (1959) 927).

Practical considerations of space limitations and finite conductor size reduce the quality of the attainable octupole field. A median plane plot of a true octupole field is shown in Fig. 2.

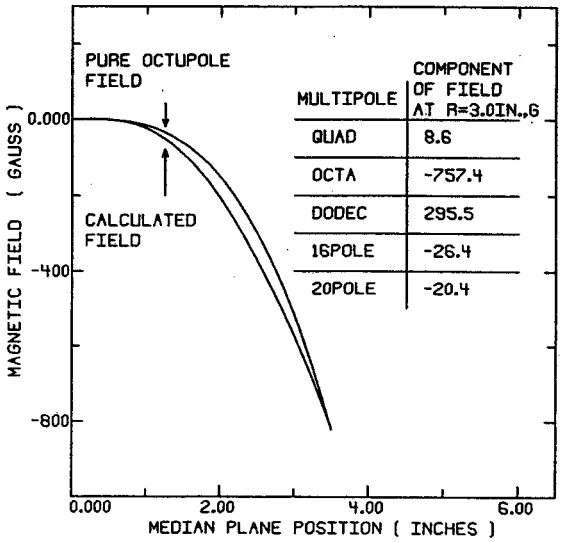

MULTIPOLE	COMPONENT OF FIELD AT R=3.0IN.,G
QUAD	8.6
OCTA	-757.4
DODEC	295.5
16POLE	-26.4
20POLE	-20.4

Fig. 2. Median plane field plot across the center of the octupole vs. a true cubic, and the multipole field components at r = 3.0 inches.

vs. the median plane field calculated from the final design of the current-sheet octupole, along with the multipole field components at r = 3.0 in. Figure 3 shows the geometry of the magnet along with the magnetic equipotential lines calculated by the program POISSON The sectioned areas represent the current carrying regions made of 1/8" square hollow soft copper conductor. The resistance of the entire coil is 0.05Ω requiring 20 volts to drive the 100A needed to produce the 500G pole-tip operating field. From the shape and symmetry of the calculated field we see the current-sheet octupole is a fair approximation to a true octupole, about 75% octupole at r = 3 in.

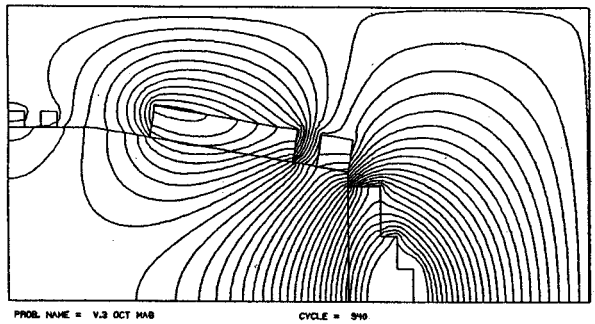

Fig. 3. POISSON calculation of the magnetic equipotential lines for the proposed octupole design. 1/4 of the entire octupole is shown. The excitation current is 100 amps.

The ultimate test, however, is the ion-optical improvements produced in the S320 spectrograph. Figure 4 summarizes the RAYTRACE calculations with B = 500G at r = 3.0 in. The error bars represent the range in focal plane position at the three values of δ for which $\frac{\Delta E}{E} = 10^{-3}$ at $\Omega = 0.5$ msr can be obtained. The spot sizes given are full base widths with a base width of 0.8 mm corresponding to $\Delta E/E = 10^{-3}$. The RAYTRACE subroutine POLES was generalized to include the higher order multipole components indicated in Fig. 2. We see the addition of the current-sheet octupole improves the resolution of the S320 spectrometer along with allowing the use of a straight focal plane detector. Therefore, the design is sufficient to meet the goals of correcting the third order aberrations, and is now planned as an addition to the spectrograph.

An additional point of interest is that the "imperfect" octupole of this design actually improves the calculated S320 line widths more than a pure octupole. That is, the higher order terms in this design happen to be of the right signs to help the spectrograph. Hence, it would have been counterproductive to carry out additional design studies of the magnet to make it more octupole in character.

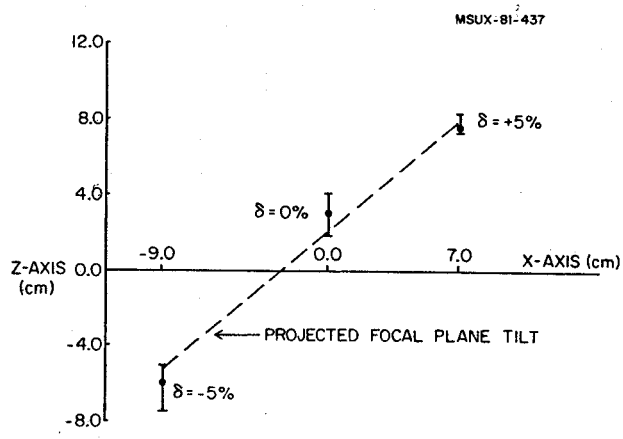

Fig. 4. Summary of RAYTRACE calculations for $-12 \text{ mr} \leq \theta \leq 12 \text{ mr}$, $-12 \text{ mr} \leq \phi \leq 12 \text{ mr}$, and $-5\% \leq \frac{\Delta p}{p} \leq 5\%$. The vertical lines represent the range for which the full base width spot size is ≤ 0.8 mm, allowing the desired $\Delta E/E = 10^{-3}$. The circle-of-least-confusion sizes, represented by the circles, are 0.77, 0.50 and 0.52 mm for δ = +5%, 0%, and -5% respectively.

Status of the RPMS

L. Harwood, J. Nolen, E. Ormand, M.S. Curtin and S. Bricker

Work on the RPMS has concentrated on the construction and testing of the prototype in the past year. Major purchases and surplus acquisitions have occurred, and detailed mechanical designs are nearly complete. A final, master series of ray-tracing calculations is near completion to give a complete description of the system's optical qualities through all orders of aberration and including aperture and slit effects. The efforts mentioned above will be described in detail below and then a prognosis for the future will be given.

Procurement: The RPMS has gained several major additions to its available components. First, from CESR came a surplus 19 ton magnet with a 15 x 45 cm aperture and a 90 cm length. This magnet will replace the K50 beamline dipole originally called for in the prototype. It will also be suitable for the Phase II design which needs a much larger gap than does the prototype. Power consumption of this magnet is very low (10 kW) at the fields needed.

The University of Maryland has given us a surplus 400 kVDC high-voltage supply, and they have also loaned us a quadrupole doublet and a 175 V, 1100 A magnet power supply. The high-voltage supply, which originally came from the Princeton-Penn Accelerator, required extensive work to make it operable. It has now been tested at 180 kV (limited by a lack of SF_6 insulating gas) with very little conditioning needed. The quadrupole doublet and magnet power supply are on loan until they are needed for the recently funded large solid-angle spectrograph to be built by University of Maryland and located at IUCF in Bloomington. The doublet will replace the second SREL doublet on the RPMS. The new doublet has a 10 cm aperture and is thus much smaller than the 20 cm SREL quads. The large decrease in mass greatly simplified the mechanical design of the moveable tail on the RPMS. The high current supply will be used to run the magnet in the Wien filter (600 A).

The only major purchase this year has been of a 400 kV DC supply for the "other" side of the Wien filter. The bids were requested, and the sole source was Spellman High-Voltage Electronics Corporation. All other suppliers put their Cockcroft-Walton stacks in an oil filled tank. The Spellman unit works in air below 200 kV and in SF_6 above 200 kV. WIth the delivery of this unit (late August) all major components of the RPMS will be at MSU.

The latest purchase was of high voltage cable. The 600 kV cable from Cable D'Lyon is rather cumbersome and difficult to work with. To minimize stored energy we plan to have the power supplies as close to the Wien filter as possible; thus we would have had to cut the 600 kV cable into shorter lengths. If, at some later time (i.e. in Phase II) we need to move the power supplies further away, then new cable would be needed. High voltage requirements will be lower in the prototype than in the final system; therefore, we have obtained some Belden 8871 cable which is rated at 200 kV DC and is relatively inexpensive ($4/ft). We can thus save the higher rated cable for Phase II.

Mechanical Design: The RPMS will be able to operate at scattering angles from 0° to 30°. The undercarriage has been designed and is currently under construction. Presently all major optical elements have been positioned on stationary supports and aligned for initial testing (see below).

The support structure for the final doublet (i.e., the "Scorpion's tail") has been built and attached to the dipole. The "tail" will be positioned with a screw-drive hoist supported on the top of the dipole. The target chamber and moveable vacuum chambers for the two dipoles have also been designed. The design for the chamber for the main dipole has been sent to an outside shop for construction. Designs for the adaptors to fit the new high voltage cable to the Wien filter and power supplies have also been completed.

System testing: Testing of the system is proceeding along two routes. First to be completed will be the final ray-tracing calculations. These calcualtions will include finite spot size, solid angle, momentum range, aperture, and slit effects. They will be done for several masses and then combined to form predicted spectra similar to those presented in last year's annual report but of higher quality. The calculations for the previous "spectra" were done by pseudo-ray-tracing with TURTLE[1] which only includes intrinsic aberrations of second order (induced aberrations are included to all orders). A set of RAYTRACE calculations for q=Z, N=Z, 20 MeV/amu ions has been completed. Rays illuminating a 1 msr aperture with an energy range of $\pm$12% were computer traced through the system. An isometric plot of the calculated peak shapes at the focal plane for $m=m_o$-2%, $m=m_o$, and $m=m_o$+2% is shown in the figure. There is 50% transmission through the 24% energy range and the base-to-base resolving power is $m/\Delta m$=100. These calculations were an undergraduate research project by David Mathews.

Testing of the real, physical RPMS will be done with an ion source presently under construction by David Mikolas. Initially attempts were made to adapt the surface ionization source developed by Dyer and Robertson[2] to this purpose, but it proved unacceptable. The purpose of the

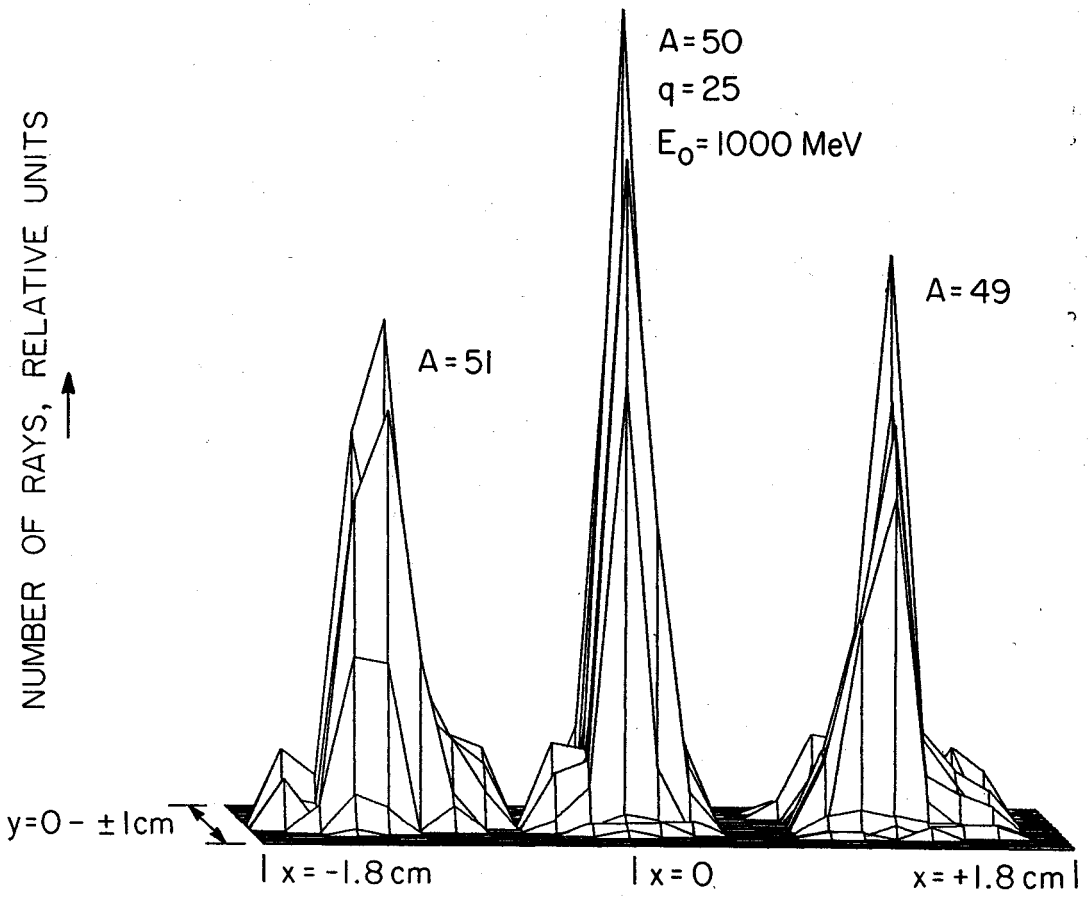

Fig. 1. RAYTRACE calculations of peak shapes at the RPMS focal plane.

source is to let us test the actual fields of the parts of the system. Specifically, we can test whether the focusing works as calculated and whether the mass dispersion behaves as predicted. All of this can be done without beam from the cyclotron. Thus, we can have the system debugged when "first beam" is available.

Prognosis: With the recent purchases, the RPMS has an essentially complete set of main components. The only significant items still lacking are the vacuum system components, all of which have been designed and some of which are under construction. Barring any unforeseen problems, the RPMS should be ready when the first beam is ready for experiments, i.e., early 1982. A focal plane array of solid state detectors for initial measurements is currently being designed.

1. D.C. Carey, private communication.
2. P. Dyer and R.G.H. Robertson, MSUCL report #346.

Prediction of Yields from Fragmentation Reactions

M.S. Curtin and J.A. Nolen

The onset of fragmentation in heavy ion reactions around 10-30 MeV/N provides a favorable mechanism for the production of exotic nuclei. A quantitative investigation of isotope yields, transverse and longitudinal momentum distributions, and angular distributions must be undertaken if fragmentation, within this transition region, is to be fully exploited for the production of exotic nuclei. The fireball model[1,2] was employed to calculate primary isotope cross-sections $\sigma(Ap',Zp')$ for projectile fragmentation specifically ^{22}Ne on ^{12}C. Figure 1 represents these cross-sections using the Hypergeometric charge dispersion relation, and Fig. 2 represents these cross-sections using the nuclear giant dipole resonance dispersion relation. Comparing the two figures gives a qualitative estimate of the uncertainty involved in these calculations. The next step in the calculation will be to obtain secondary isotope distributions via the use of a cascade code. However, a necessary input for the cascade code is the excitation energy of the primary fragment, which for light nuclei is not as transparent as for heavier nuclei. In order to predict angular distributions within this 10-30 MeV/N energy domain one must first calculate the variance in the transverse momentum distribution. According to Van Bibber et. al.[3] the variance of the transverse momentum distribution is considerably larger than predicted by just taking into account the Fermi motion of the projectile nucleons. This increased variance is due to orbital deflection occuring before fragmentation and thus is sensitive to the incident projectile energy.

---

1. J. Gosset, H.H. Gutbrod et. al., Phys. Rev. C16 629 (1977).
2. G.D. Westfall, J. Gosset et. al., Phys. Rev. Lett. 37, 1202 (1976).
3. K. Van Bibber, D.L. Hendrie et. al., Phys. Rev. Lett. 43, 840 (1979).

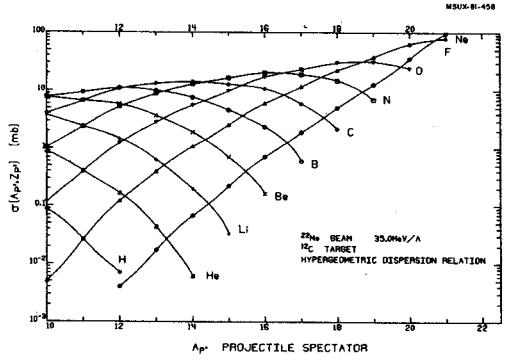

Fig. 1

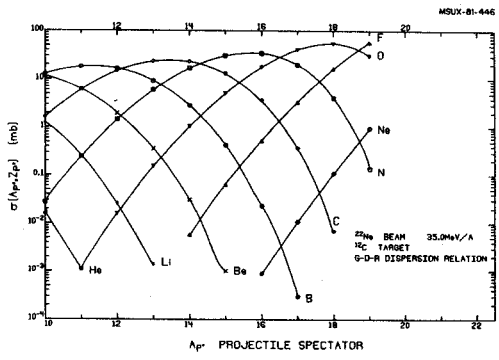

Fig. 2

Study of Induced Aberrations in Ion Optics

L.H. Harwood and J.A. Nolen

In the course of making ion optical designs for the various devices we are working on, we have often discovered that a particular design which was very promising after second order correction would turn out to be totally unacceptable when third and fourth order induced effects were included. These "induced" effects are aberrations which arise from cross terms in the Taylor series and are not due to intrinsic aberrations of any one device. For example, consider a system, AB, made up of two sections, A and B, with B following A. Assume with no correcting elements AB has only one second order aberration and none of higher order. Sextupoles are then added to A and B such that the second order matrix of AB is zero. In all probability, A and B will each have some second order aberrations due to the correcting sextupoles; for this illustration assume A has an (x/x^2) aberration and B has (x/x^2) and $(x/x\theta)$ aberrations. The system AB will have at least two aberrations above second order even if neither A or B had them. These aberrations are $(x/x^2\theta)_{AB} = (x/x\theta)_B(x/x^2)_A$ and $(x/x^4)_{AB} = (x/x^2)_B(x/x^2)_A^2$ (Note: Subscripts indicate the section to which the aberration pertains.)

Such "induced" aberrations can, as stated above, have disastrous effects and are quite insidious because the process of correcting second order aberrations can quite easily generate very large "induced" terms. Ion optical designs often terminate at second order because until recently[2] no third order matrix code was available and ray-tracing is very time consuming. Thus, it is quite easy to have a design that looks good at second order but is, in fact, useless at the desired solid angle.

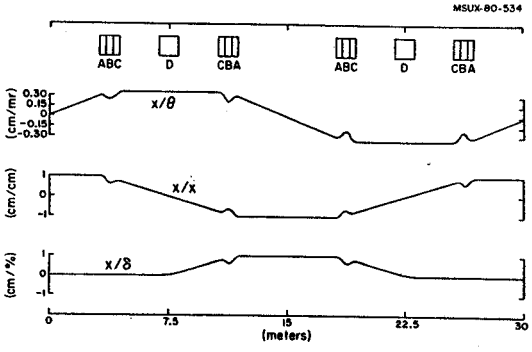

Fig. 1. Schematic of first-order optics of the test system. The y/y and y/ϕ rays are similar to the x/x and x/θ rays since the focusing conditions are the same for both planes. The labels under the elements indicate how each is energized. Any two elements with the same label are energized identically. A, B and C are combined quadrupoles and sextupoles, and D is dipole. A and C have the same sextupole components.

To investigate these induced aberrations, a test system was used. The layout of the system is shown in Fig. 1 along with the first order optics. This system could be considered part of a beam transport system; it is also similar to the optics for the proposed Phase II Reaction Product Mass Separator.[3]

The first investigation was of the line width dependence on solid angle, momentum band pass, and dispersion at the center of the system (dipole bend angle). For each dispersion the sextupoles were readjusted to exactly cancel all second order aberrations. Figure 2 shows the results for a momentum range of 10%. The ordinate is the dipole field (which is directly proportional to the dispersion). The strong dependence of the line width on solid angle and dispersion is evident. Notice that the optimum dispersion (magnetic field) increases monotonically with the solid angle. This is more evident in Fig. 3 where we show the results for all the calculations.

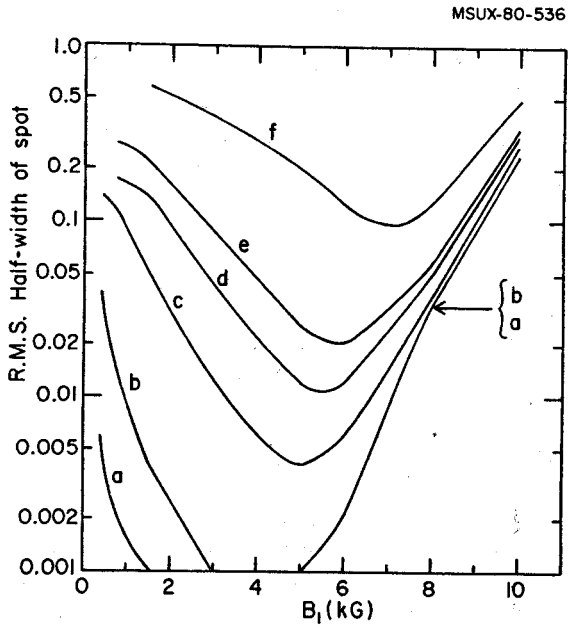

Fig. 2. Line width versus dipole field is shown for the corrected test system. The various curves are for different solid angles. The momentum acceptance is held constant at 10%. Note that there is a minimum in each curve. The θ and ϕ ranges are equal for each curve and are: (a) 1 mr; (b) 2 mr; (c) 5 mr; (d) 7.5 mr; (e) 10 mr; and (f) 20 mr.

We remind the reader that all effects observed are of third and higher order because the second order aberrations have all been corrected. While it is in principle possible to correct these higher order aberrations with octupoles, decapoles, etc., there is no guarantee that the series will converge.

MSUX-80-535

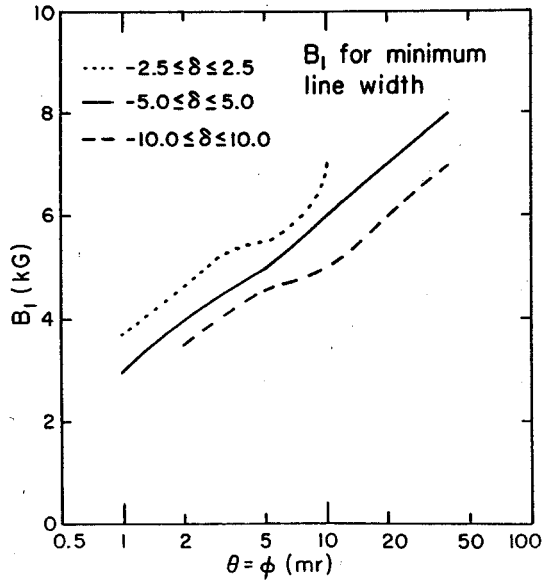

Fig. 3. The positions of the minima in the line width versus dipole field are shown. These positions were obtained from Fig. 2 and other plots for 5% and 20% momentum ranges.

We suggest that whenever possible the bend angles of dipoles not be rigidly fixed until after the third and higher order aberrations have been investigated. We (and others)[1] have found that the minimum line width often occurs when $(x/\theta)\theta_{max} = (x/\delta)\delta_{max}$ in the vicinity of correcting sextupoles and suggest that others try this rule-of-thumb.

Of course it is not always possible to meet the above condition. Therefore we tried to find if it is possible to improve a system which is not optimized and do it in a simple way. We reasoned that if no sextupoles give predominately second order aberrations and "full strength" sextupoles give no second order but large third and higher order terms, then at some intermediate sextupole strength we might decrease the sum of all aberrations relative to either extreme in sextupoel strength. This was sometimes in fact the case, as illustrated in Fig. 4. These calculations have an optimum dipole field of 5 kG. Thus, its minimum should be at a scaling factor of 1.0. At 3 kG, the minimum is still at a scaling factor of 1.0 but is not so deep as that for 5 kG.

MSUX-80-537

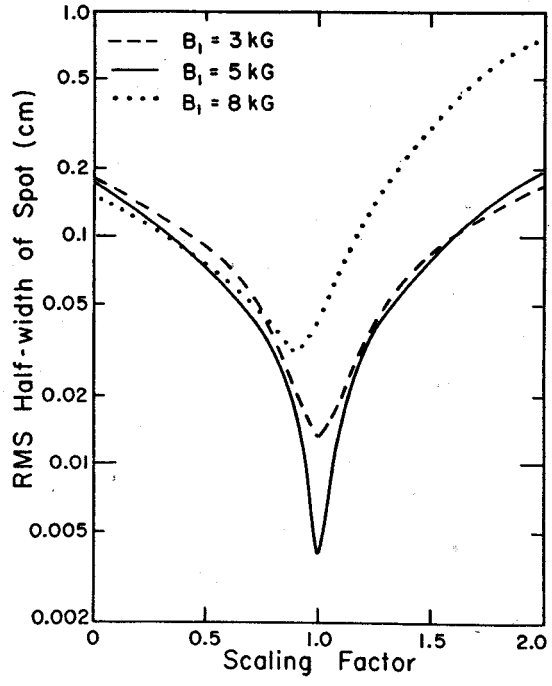

Fig. 4. The effect of scaling the sextupoles is shown. Note that the curves for B_1 = 3 and 5 kG have minima at a scaling factor of 1.0. The B_1 = 8 kG curve is minimum at a scaling factor of 0.9.

The 8 kG curve, on the other hand minimizes at scaling factor of 0.9. We have decreased the higher order terms more than we have increased the second order. We therefore suggest that designers keep in mind that the goal is usually to get a minimum line width and not to have a "perfect" second (or third) order correction. If a system can be improved by relaxing the usual stringent "no second order aberrations" requirement then it should be relaxed. Specifically, we suggest scaling all the sextupole strengths until a minimum line width is achieved.

A more detailed discussion of the above ideas and related concepts can be found in ref. 1.

---

1. L.H. Harwood, J.A. Nolen, Jr., and K.L. Brown, Proceedings of the Conference on Charged Particle Optics, Giessen, Sept. 8-12, 1980, to be published, NIM.

Resolution Limits of the k-800 Spectrograph

A.F. Zeller and J.A. Nolen

In addition to the resolution inherent to spectrographs and detectors themselves, contributions to broadening are possible from the nonzero emittance of the beam and from effects in the target itself. The effects of multiple scattering, straggling and target nonuniformities, as well as the effects of beam divergence, depend strongly on the reaction and the incident energy. Generally the resolution effects are proportional to the kinematic parameter, k,

$$k = \frac{1}{p}\frac{dp}{d\theta}$$

Since heavy ion reactions tend to have large values of k, small polar acceptance angles are usually required, even at forward angles. However, this problem can be compensated for, in varying degrees by ray tracing with multiple detector systems or by spectrograph compensation techniques

Energy Loss Straggling

Contributions from straggling are calculated from the formula due to Bohr[1]:

$$E = 30 \times Z_p\left[\frac{Z_T \times T}{A_T}\right]^{\frac{1}{2}} \quad \text{keV (FWHM)}$$

where T is the target thickness in mg/cm^2, which gives E in keV for target mass and charge, A_T and Z_T, and projectile charge, Z_p.

Target Nonuniformity

Broadening due to non-uniformity in the target is directly proportional to the target thickness and the degree of nonuniformity. For the lighter heavy ions at high energy using targets of approximately 1 mg/cm^2 the contribution due to this effect is small. Generally for targets like carbon, nickel, gold, etc. in the thickness range of 100-300 μg/cm^2 uniformities of approximately 5% can be obtained by careful preparation. For targets of 1 mg/cm^2 and up, a reasonable estimate is perhaps 10% uniformity. Using only a small region of the target can, of course, reduce the nonuniformity contribution, at a cost in beam intensity (with a spot size collimator) or increased beam divergence (focussing to a small spot). The choice of operating conditions will be dependent upon the specific experiment, as will become apparent in the examples shown later.

Multiple Scattering in Target

The contribution due to multiple scattering in the target is given by:

$$E = 4 \times E_3 \times k \times \theta_{\frac{1}{2}}$$

where $\theta_{\frac{1}{2}}$ is the half angle for multiple scattering on a target of T μg/cm^2, calculated from a modified equation[2] due to Meyer[3], and E_3 is the energy of the outgoing particle.

Beam Divergence

The broadening due to beam divergence is also given by the equation immediately above, but here $\theta_{\frac{1}{2}}$ is the beam divergence half angle on target. In spectrographs which disperse in the scattering plane this term can be compensated for by returning the beam to focus off the target. In this case kinematics and dispersion matching are interrelated and the beam must be refocussed at each scattering angle as the kinematic parameter changes. In spectrographs which disperse perpendicular to the scattering plane (such as the present case) this term cannot be compensated for directly. However, in practice it can be reduced significantly by using a wide beam spot with narrow divergence in the scattering plane. This does not affect the energy resolution otherwise because the dispersion is in the other plane.

Sample Reactions

As examples of likely reactions, we will examine the elastic scattering of ^{16}O, ^{40}Ar, ^{40}Ca and ^{86}Kr on ^{28}Si, ^{40}Ca and ^{208}Pb targets at energies chosen that will be available from charge states having sufficient intensity to make an experiment feasible.

A saving feature of these high energy reactions is that the grazing angle, i.e., the region of most interest, is very far forward, in the region of 1-5°. This means that the value of the kinematic parameter, k, is reasonably small and those effects which depend on k are also reduced. Non-relativistic optical model calculations with the code JIB,[4] modified to allow use of 300 partial waves, have been made for some representative systems, using parameters available in the literature for measurements made at lower energies. Figure 1 shows a calculation for the $^{28}Si(^{16}O,^{16}O)^{28}Si$ system at 960 MeV (60 MeV/A) using parameter set E18 from ref. 5. Note that the angular range of interest is less than 10° in the lab, but that angular resolution is very important--requiring a resolution of 0.15° (i.e., 2.5 mr), perhaps more critical than the energy resolution requirement (1.78 MeV).

Figure 2 shows a calculation for the $^{40}Ca(^{40}Ca,^{40}Ca)^{40}Ca$ system at 20 MeV/nucleon made using the parameters from ref. 6. It is clear that again very good angular resolution is needed.

Results

Table I lists various reaction systems likely to be run in phase II. Reactions at a range of beam energies are included. The beam divergence is consistent with projected operation and target thicknesses are likely numbers, chosen to give

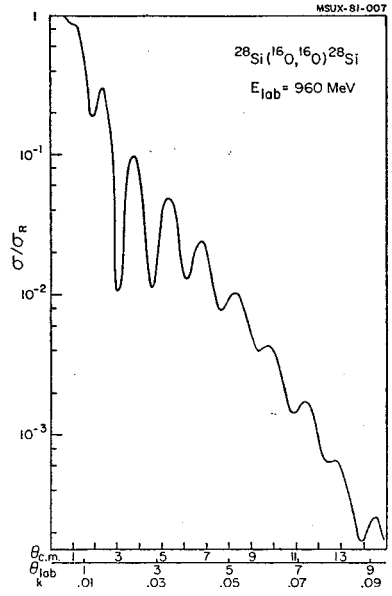

Fig. 1. Optical model calculations for $^{28}Si(^{16}O,^{16}O)^{28}Si$ at 60 MeV/A.

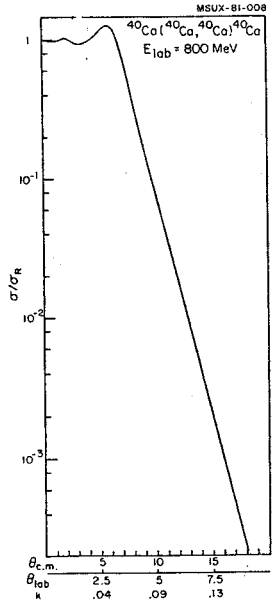

Fig. 2. Optical model calculations.

reasonable values for uniformity and straggling contributions. Target thicknesses have not been adjusted in each case to obtain optimum contributions to overall resolution. It is obvious from Table I that the non-uniformities contribute little to the broadening, except at low energies, and a factor of two increase in this term would not degrade the expected resolution significantly, since the total resolution is the quadratic sum of the individual contributions.

Listed in the last column of Table I are the excitation energies of the first excited states in the reaction systems. This is assumed to be the minimum resolution needed so that by peak-fitting elastic scattering angular distributions can be obtained.

Looking in detail at Table I, it is obvious that for high energy beams (about 6 to 10 Gev) the intrinsic resolution of the spectrograph system ($E/\Delta E$ = 10,000) is the dominant contribution to the resolution. Only when the lighter beams, e.g. ^{16}O to ^{40}Ca, at energies less than the maximum available are used do target effects such as straggling and multiple scattering become prominent factors. Of course, at more backward angles or reactions on light targets, when the kinematic parameter, k, is large, effects which depend on k produce large contributions.

Effects other than those discussed here may be significant, too. For reactions other than elastic scattering, where charge transfer occurs, for example, differences in energy loss in the target may become a dominating factor in the resolution. If the 40 MeV/A ^{40}Ar undergoes a charge transfer of 2, a contribution due to the energy difference leads to a 300 keV effect. At higher energies this effect is less significant because of the reduced energy loss in the target.

It is evident from Table I that the intrinsic resolution of the spectrograph systems, including the detector systems, represents the dominant component in achieving the best resolution at the high beam energies (40-200 MeV/A) which are possible with MSU Phase II. Target thickness effects usually dominate energy resolution in spectrograph experiments with lower energy heavy ion beams (5-20 MeV/A), but such is not the case at the higher energies. Thus effort in spectrograph design will produce significant rewards in terms of energy and angular resolution which far outweight expenditures in trying to reduce other contributions to the resolution.

1. N. Bohr as used in Introduction to Nuclear Physics, H. Enge (1966), p. 188.
2. R.M. DeVries, private comm. (1979).
3. L. Meyer, Phys. Stat. Sol. 44, 253 (1971).
4. F.G. Perey, Phys. Rev. 131, 745 (1963); and A.W. Obst, FSU report, unpublished.
5. J.G. Cramer et al., Phys. Rev. C14, 2158 (1976).
6. H. Doubre et al., Phys. Rev. C15, 693 (1977).

Table I. Calculated Resolution

Reaction	E_{lab} (MeV)	E/A	K[a]	Target Thickness (non-unif) (mg/cm^2)	θ_{graz} (deg) (cm)	θ_{lab} (deg)	θ_{cm} (deg)	$k\left(\frac{1}{p}\frac{dp}{d\theta}\right)$	ΔE^b BEAM (kev)	ΔE MULT. SCATT. (kev)	ΔE STRAG (kev)	ΔE Non-Unif (kev)	ΔE^c SPEC (kev)	ΔE Total (kev) (FWHM)	E^{*d} (kev)
$^{28}Si(^{16}O,^{16}O)$	960	60	240	1±.1	1.4	1	1.6	0.010	12	10	170	56	96	204	1780
						10	15.9	0.103	123	100			94	257	
$^{208}Pb(^{16}O,^{16}O)$	3200	200	800	5±.5	1.2	1	1.1	0.0015	6	6	337	74	320	471	2615
						10	10.9	0.015	59	59			319	477	
$^{208}Pb(^{40}Ar,^{40}Ar)$	1600	40	198	1±.1	5.6	3	3.6	0.010	20	30	339	234	160	444	1460
						15	18.0	0.051	101	150			160	477	
	6400	160	790	1±.1	1.4	1	1.2	0.0036	29	11	339	86	640	730	
						10	12.2	0.036	289	107			640	788	
$^{40}Ca(^{40}Ca,^{40}Ca)$	800	20	80	0.1±.005	6.6	7	14.1	0.124	124	70	134	40	80	214	3348
	8000	200	800	0.1±.005	0.7	1	2.1	0.019	192	11	134	7	800	834	
						10	21.0	0.195	387[e]	110			780	888	
$^{208}Pb(^{86}Kr,^{86}Kr)$	11180	130	742	0.1±.005	1.7	1	1.5	0.0077	107	6	214	24	1118	1144	1560
						10	14.5	0.077	214[e]	65			1103	1146	

a) rigidity parameter for fully stripped ion

b) assumes a beam divergence (full angle) of 1 mr

c) assumes an $E/\Delta E=10^4$

d) excitation energy of 1st excited state of target or projectile, i.e. required resolution

e) assumes a beam spot in the scattering plane 5 mm x 0.2 mr which could be obtained by not rotating phase space and refocussing at the beam analysis object slits.

Dipole Design Studies for the k=800 Spectrograph

A.F. Zeller, J. Nolen and L.H. Harwood

Magnet design calculations were performed with the code POISSON[1] using a permeability curve that is typical for a 1006 steel (carbon $\leq$ 0.08%). The bases for comparing designs were the region of good field (previously defined[2] as the region with a field gradient less than $\pm$ 1 G/cm) and the constancy of the field quality over a wide range of field strengths, typically 5-15 kG.

The dipole designs considered in this report are window-frame magnets with superconducting coils. In these studies the magnet steel is at room temperature and the coil cryostat is in the magnet gap. To allow room for the cryostat the coil must be shorter than the gap height. Such a "concentrated" coil tends to give too strong fields near the coil; this is partially compensated for in most of these studies via the use of a very thin pole-tip (~few mm). In searching for the optimum design, the pole-tip thickness was one of the variables. Other variables were the position of the coil, the coil shape and the use of vertical slots in the yoke. The window-frame geometry normally provides a field that increases radially, i.e., a positive gradient. This is shown in Fig. 1 as the curve labelled "1". Other designs shown in the figure give the corresponding gradients. It is of interest to note that the basically window-frame coil geometry, with the addition of a small pole and a vertical slot, gives a gradient characteristic of an H-frame.

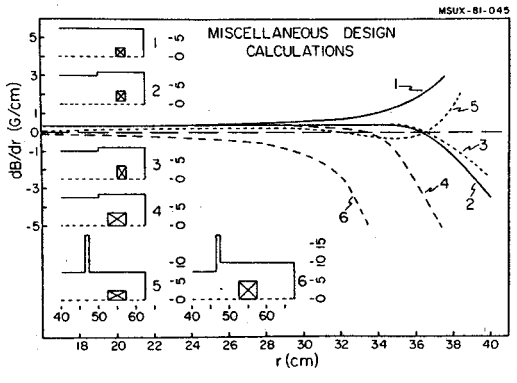

Fig. 1. Miscellaneous design calculations.

A more detailed study of the effects of the slot is shown in Fig. 2. The pure window-frame field (no slot) is changed to an H-frame field by addition of the slot. The curve #4 shows that the position and height can be optimized to considerably extend the region of useful field.

The effects of changes in the pole tip thickness are shown in Fig. 3. The curves labelled with only the pole thickness (in cm) are for a central field of 15 kG. The (5) after the pole thickness indicates a calculation at a central field of 5 kG. The desired conditions are for both the 15 and 5 kG solutions to give 35 cm of good field, thereby providing a spectrograph with a wide range of useful B fields.

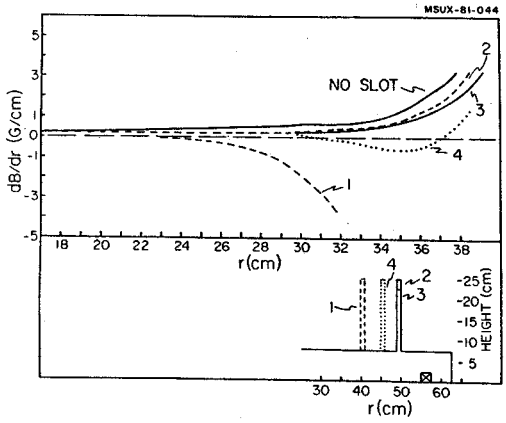

Fig. 2. The effects of vertical slots.

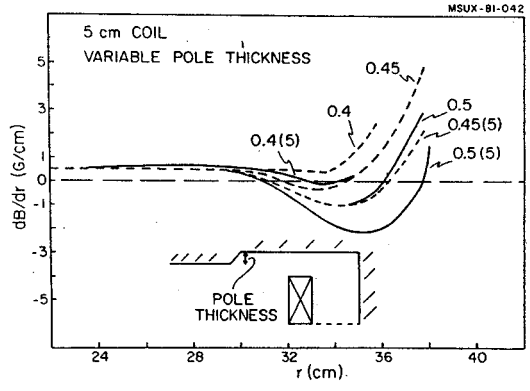

Fig. 3. The effects of changes in the pole thickness.

For a given pole thickness, coil height variations cause changes in the field profile as shown in Fig. 4. A more concentrated coil, i.e., the 3.5 cm one, produces essentially a pure window-frame profile, despite the pole piece; while the 5.5 cm one provides a window-frame gradient to ~28 cm before falling off as an H-frame. This feature of coil height variablility provides an excellent control on field shape.

Once an appropriate combination of pole thickness and coil height is found, it is fine tuned to produce a design which provides the widest range of useful fields Figure 5a shows the current design over a wide range of excitation. The μ_∞ curve is for infinite permeability at a central field of 15 kG. The overall cross section is shown in Fig. 5b. This magnet weighs ~50 tons.

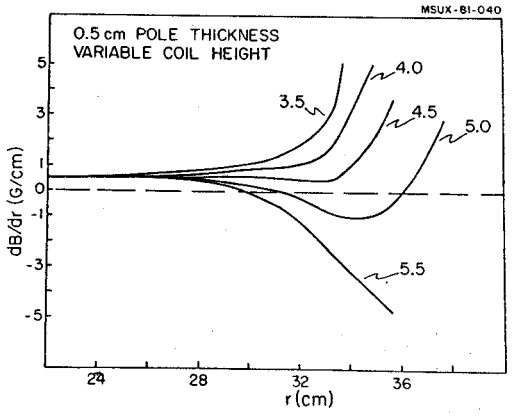

Fig. 4. The effects of changes in coil height.

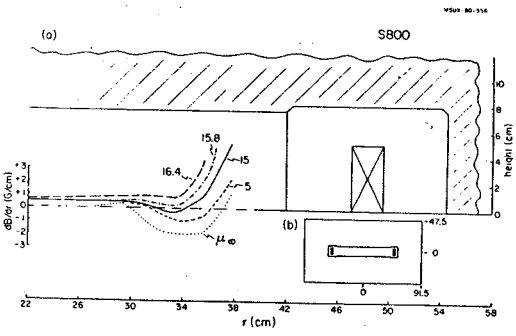

Fig. 5. a) Enlarged cross section of the coil region and gradients for several fields.
b) Cross sectional view.

Cylindrical coordinate calculations were done to optimize the widths of the side yokes in order to make the physical center of the magnet coincide with the position where the field gradient changes sign. Removing 2 cm from the outer yoke and adding 4 cm on the inner fulfills this criterion. Generally, however, the extent of useful field did not depend strongly on the relative widths of the side pieces.

Since there is no way of knowing the exact permeability curve for the iron, sensitivity to permeability was examined. Figure 6 shows the results of changing from a μ_{max} consistent with 1006 steel (μ_{max} = 2200) to a commercial 1015 steel (μ_{max} = 1500) for different fields. Thus even this worst case does not seriously degrade the design.

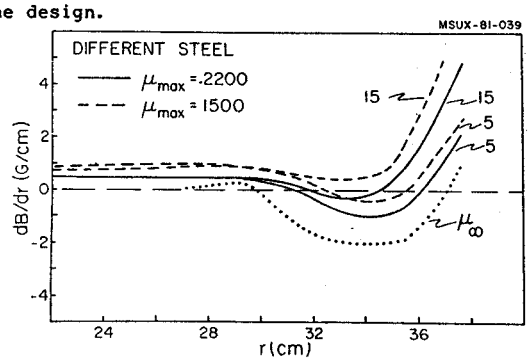

Fig. 6. The effects of different permeability curves.

These designs involve superconducting saddle coils which may be expensive to build. This problem is being investigated; at the same time, alternate, slightly more massive dipole designs with simpler coil structures are being considered. The choice for the S800 dipoles will be made after several cost analyses are completed.

1. R.F. Holsinger, program POISSON (unpublished) 1979.
2. MSU Annual Report 1979-80, p. 78 (unpublished).

Gamma-ray Beam Line and Goniometer System

R.M. Ronningen, R. Blue, J. Kasagi, A.F. Zeller

Late in the Fall of 1980, the wall plug for the γ-ray beam line was installed and construction of the line began. By the end of February, 1981, a quadrupole doublet, an ion pump, two carefully aligned beam boxes, a 6-inch gate valve, and beam tubes were assembled to form a 20 ft section of the beam line. To date, a cryopump, the goniometer, and the target chamber have been added and vacuum-tested.

The γ-ray beam line and goniometer[1] system is located in the south vault of the Phase I experimental area between the beam lines for the cryogenic helium-jet and the RPMS. A relatively lengthy beam line was chosen so that detection equipment at the goniometer site is in a region of reduced residual background, which may originate from the RPMS or He-jet target areas or from an external beam dump on the γ-ray line. Yet, ample space is provided downstream of the goniometer. The distance from the wall upstream to the target position is about 27.0 ft. and from there the distance to the downstream wall is about 19.0 ft. Thus larger arrays of detectors and/or auxiliary devices (e.g., large NaI crystals) can be placed leaving a comfortable distance to a remote Faraday cup/beam dump (still in its design stage). The distance to the nearest, co-parallel, shielding wall is about 4.55 ft. Figures 1 and 2 show the goniometer and upstream beam line at present.

A signal cable patch panel is being installed conveniently to the goniometer position and will have sizable numbers of signal (30), low-noise (20) and H.V. connections (20). Water, air, dry-nitrogen, and power utility outlets are also in close proximity.

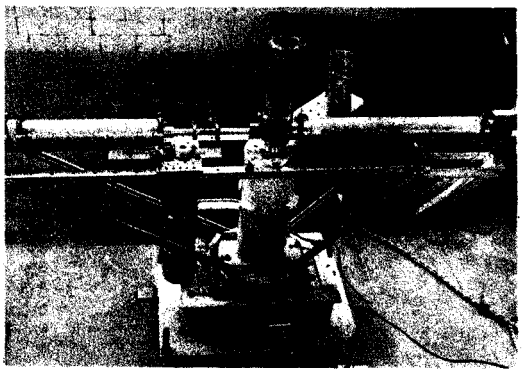

Fig. 1. Goniometer with central target chamber. An auxillary chamber is shown at the extreme right.

The upstream beam line is shown in Fig. 2. The quadrupole doublet is about 16.5 ft. from the upstream dipole magnet and about 20 ft. from the target. Beam transport calculations shown

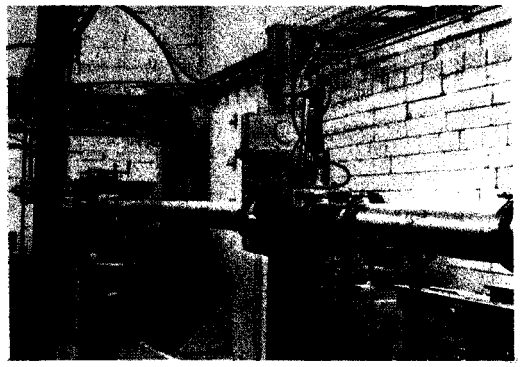

Fig. 2. Gamma-ray beam line upstream of goniometer.

that for a beam of about 20 MeV/A spot sizes under 2.5 mm are achievable. For beam diagnostics an air piston-driven scintillator in the beam box closest to the target, about 6.4 ft. from the target, can be viewed by a television camera. The beam may be steered horizontally by the dipole magnet, and vertically by a small magnet (~370 G) located in the beam box nearest the quad doublet. The two beam boxes contain vacuum diagnostic equipment (Bourdon, thermocouple, and ionization gauges) as well. But, they serve also as alignment points as they are carefully aligned to the 0.7° bend from the dipole magnet and to the proper height.

It is expected that the beam line upstream of the 6 in. gate valve (see Fig. 2) will normally be kept under high vacuum conditions. All (save 1) vacuum seals use indium wire or grease-free Viton O-rings. With the 100 l/sec ion pump on this section (about 20 ft.) a pressure of about 1×10^{-7} Torr (at the pump) has been achieved. After this gate valve a cryopump provides high vacuum for the target chamber and downstream plumbing. A pressure of about 3×10^{-7} Torr has been achieved in the beam box near the cryopump. The entire beam line, from wall plug to the 4 in. central target chamber in terms of vacuum is ready to accept a beam.

K500 Magnet Mapping with Trim Coils and Extraction Elements

P. Miller, D. Poe, H. Laumer, H. Blosser and D. Johnson

The K500 magnet was dismantled in spring of 1980 to install trim coils and to make penetrations through the midplane sections of the coil and cryostat for extraction elements. Some iron shims were also added and removed to adjust the average field and the flutter according to calculations with previously measured field maps. After these installations, the re-assembled magnet was field mapped again starting in January 1981. These maps are the data for predicting the main coil currents, trim coil currents and focusing bar positions needed for any beam. The mapping apparatus measured the field with an accuracy of approximately $\pm$ 10 G. This figure is dominated by the estimated effect of slow unpredictable changes in the calibration constants for the flip coils which occured continuously.

The operating region of the cyclotron, between B_o = 30 kG and B_o = 49 kG (B_o = central magnetic induction) was covered with a grid of 15 points in the coordinate plane defined by the currents in the small and large main coils, called I_α and I_β respectively. The accuracy of interpolation in this size grid was verified experimentally. It was necessary to develop a standard turn-on cycle to avoid a small hysteresis effect in the radial profile ($\lesssim$20 G). A short circuit developed during operation at the highest excitation (I_α/I_β = 600 A/800 A) which persisted thereafter but had no measureable effect on the steady state field of the magnet, although it constrained the current rampings to be slower than usual to limit the axial forces in the coil support links.

The trim coils were mapped at 4 main excitations near the corners of the base field grid. Hysteresis effects from main coil or trim coil excitation on the trim coil - produced field were found to be negligible. The average field from each trim coil was slightly larger than the calculated field assuming air core coils and varied a few percent with excitation, presumably due to saturation of the yoke. Figure 1 shows an example of the experimental and air-core average fields.

The passive magnetic channels were designed using surface current (saturated iron) calculations of the field perturbations that they produce. These calculations were verified experimentally in two ways:

1) The total change in field caused by the focusing bars was displayed by subtracting a field map (point by point) measured without focusing bars in the magnet from a map taken at the same coil currents after installation of all the focusing bars in their center positions. This was compared directly with the field calculated by the surface current representation of the bars (see Fig. 2).

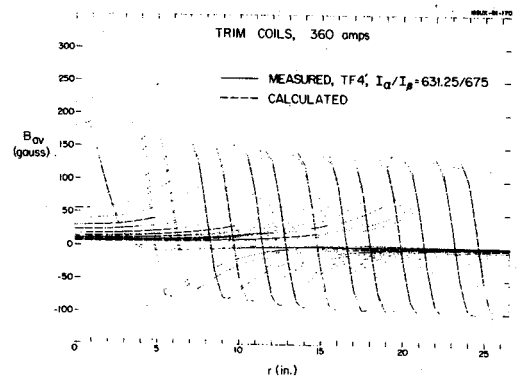

Fig. 1. Trim coil average field measured at I_α/I_β = 631.25/675 amps (B_o = 46.0 kG) and calculated (air core coils).

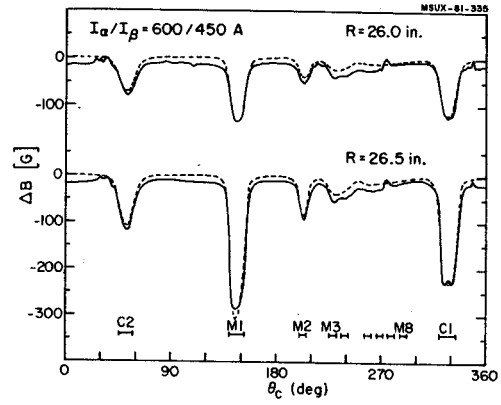

Fig. 2. Magnetic field perturbation ΔB due to installation of focusing bars M_1-M_8 and C_1 and C_2 (compensators) at the radius of the outer flip coil (R = 26.5 inches) and the adjacent one. Solid curve was measured, at I_α/I_β = 600/450 A (B_o = 39.1 kG) dashed line is the calculation (surface current). The abscissa is the azimuth relative to the cyclotron reference. The zero shift of about 12 G is from a slight difference in I_α between the two maps subtracted.

2) The changes in the field map that occurred when one or more focusing bars were moved radially outward by 0.25 inch was compared with the changes expected from the calculation. An example of these data is the graphs in Fig. 3.

Both methods show that the calculations accurately portray the field perturbations produced by the focusing bars inside the extraction radius. The first harmonic compensation is successful at all radii out to the extraction point; the second harmonic was not compensated in the design (see Fig. 4).

The shape of the edge field (R>26.5 inches) was inferred from measurements at 5 azimuths where holes exist in the median plane so the field measuring probe could be displaced radially into the coil. The field modulation was taken into account, and the average field in the region

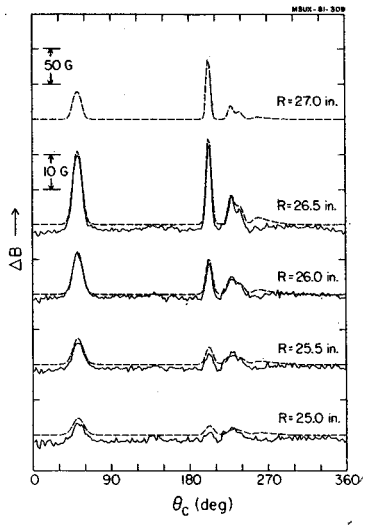

Fig. 3. As in Fig. 2 except field perturbation is due to a +0.25 inch radial displacement of the elements M_2-M_8 and C_2. Measurements were made with I_α/I_β = 662.5/550 A (B_o = 43.1 kG).

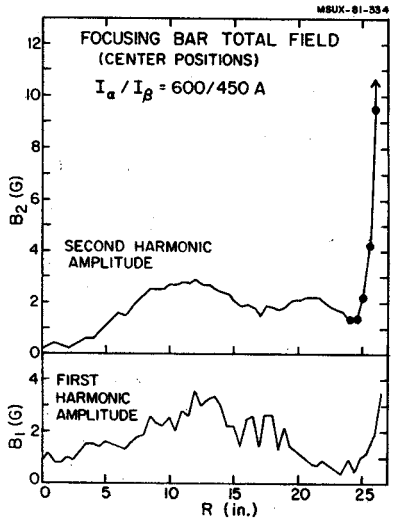

Fig. 4. First and second harmonic amplitudes of the total focusing bar fields (data as in Fig. 2).

27 in. $\leq R \leq$ 40 in was obtained for each of the base fields. This allows the total field to be calculated at any azimuth along the trajectory of the extracted beam out to R=40 in. to an estimated accuracy of $\pm$50 G.

Central Region Studies

F. Marti, M.M. Gordon, C. Salgado and D. Clark

Modifications of the electrolytic tank

To determine the accuracy of the electrolytic tank facility we did extensive measurements on a test tank. The test set-up consisted of two cylinders, one contained inside the other.

We measured the potential distribution in the region between them as shown in Fig. 1. The theoretical potential distribution is given by a fairly simple analytic expression. This test showed that the tank results were not as accurate as we desired (1%). The difficulties were attributed to the self-balancing bridge electronics. Jack Jenkins and the electronics group modified it to make it D.C. coupled, and thereby eliminated the troublesome reactive component of the balance criterion that was previously introduced by the D.C. blocking capacitors. With the new electronics the measurements were verified to be within one percent (of the applied voltage difference) of the theoretical values. As a result, the scanning speed of the tank could be doubled.

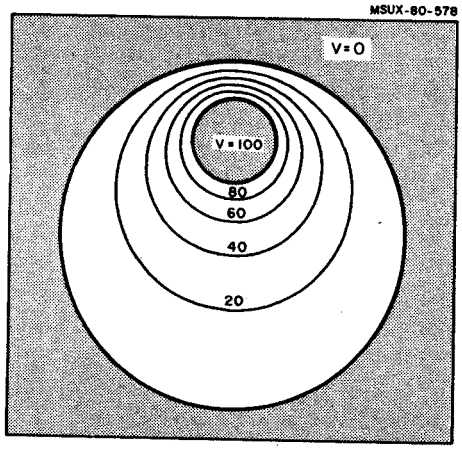

Fig. 1. Electrolytic tank test set-up. Equipotentials derived from a measurement. The discrepancies between measurement and theory are within one percent of the potential difference applied between electrodes.

Source to puller measurements

Due to the importance of knowing as accurately as possible the motion of the ions between the source and the puller, our orbit code uses a special electric field in this region, measured in an enlarged model(5:1), compared to the model used for the rest of the central region (1:1 scale). Our previous computations were done with just a 2-dimensional model. In that model the puller was defined by two thin cylinders and because the equipotentials close to the puller encircled these cylinders, it was impossible for the ions to gain the maximum energy without striking the puller.

To eliminate this problem we have constructed realistic three-dimensional models (Fig. 2). This has been done for both first and second harmonic source-puller regions. The distance between source and puller in second harmonic is 80 percent of the first harmonic case, but the puller aperture is not decreased proportionately.

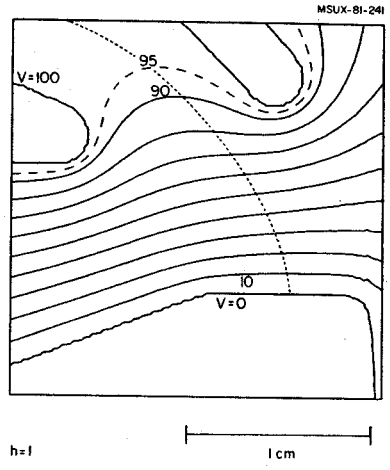

Fig. 2. Source to puller geometry for h=1. Equipotentials obtained in the region between ion source and puller for first harmonic operation using a tridimensional five to one scale model. The dimensions shown here correspond to the actual size in the cyclotron. The dotted line indicates the orbit of the central ray particle described in Fig. 3.

First harmonic central region

A final design of the central region for first harmonic operation was achieved. The total number of turns is 530. To minimize the number of changes in the central region electrodes, it was decided to keep the turn number fixed. This will be achieved by varying the dee voltage.

Figure 3 shows an example of a typical ion accelerated in first harmonic, and Fig. 4 shows the phase behavior during the first 15 turns.

Second harmonic central region

As explained in last year's annual report, the distance from ion source to puller in second harmonic operation is only 80 percent of the distance in the first harmonic case (to compensate for the increase in transit time). The total number of turns will be approximately 260, requiring consequently a completely different set of electrodes from those used in first harmonic.

We have achieved a final design that satisfies all our requirements for good centering, focusing, and electrode clearance. Figure 5 shows the central ray of the test ion. Figure 6 shows the actual equipotentials in second harmonic operation.

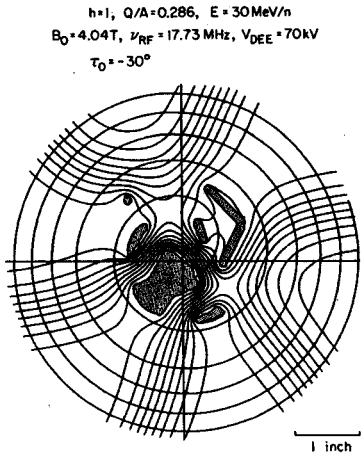

Fig. 3. Central region for h=1 (530 turns). The ion source and electrodes penetrating the median plane are shown as shaded areas. The equipotentials shown here correspond to all three dees having the same voltage (third harmonic) and clearly indicate the outline of the six gaps. Note that for first harmonic operation, the three dees have voltages which are 120 deg out of phase. Thus, the static potential shown here is not the actual one, but only a simple superposition which is useful for outlining the electrodes and gaps. Superimposed on the equipotentials is the orbit for the central ray of the beam ($^{14}N^{4+}$) having the given parameters. This orbit emerges with a centering error of about 40 mils. This ion spends only five turns in the region covered by the measured potentials. The parameter τ_0 is the starting time (in rf degrees) of the ion relative to the peak voltage between ion source and puller. Time is more positive for a later particle.

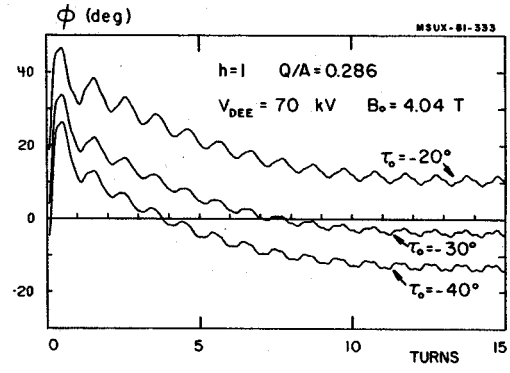

Fig. 4. Local phase for h=1 (530 turns) orbits. Evolution of the local phase for three ions starting 10 rf degrees apart from the source. Observe the 30 deg phase swing produced by the central magnetic cone. These curves show the once per turn oscillations ($\nu_r \approx 1$) characteristic of off-center orbits. (These orbits finally emerge with center displacements of 70, 40 and 60 mils reading from top to bottom.) In addition, a thrice per turn oscillation can be observed starting at about eight turns as a result of the three sector orbit scalloping. When these ions reach turn n=15, the average radius is about 4.5 inch.

Examples of our studies of radial phase space behavior are shown in Figs. 7 and 8.

Vertical motion

Since the z motion code is completely linear, the general solution, and hence the transfer matrix, can be generated from any two independent solutions like those shown, for example, in Fig. 9. An auxiliary program has been developed which evaluates this transfer matrix as a function of θ, and then uses it to determine the maximum vertical acceptance (area of phase space ellipse) for a given central ray orbit. For a group of orbits whose initial (z,p_z) values completely cover this ellipse, the program then finds the vertical envelope (maximum value of z) as a function of θ, and this envelope (an example of which is also shown in Fig. 9) reveals quite clearly the quality of the vertical focusing at different places in the central region.

Figure 10 shows an expanded view of the first three turns which clearly reveals the "noise" in the p_z curves. The relatively low level of this noise gives us some confidence in the potential measurements obtained from the electrolytic tank.

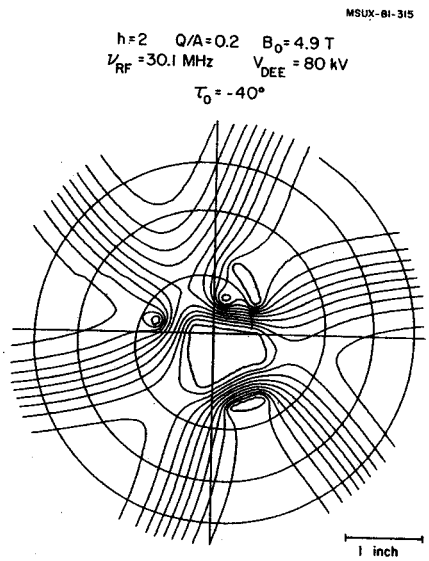

Fig. 5. Central region for h=2 (260 turns). The central ray of the beam shown here finally emerges with a centering error of only a few mils. Note that the electrodes and ion source are substantially different from those used for first harmonic. When changing modes of operation, the tips of the dees will be removed or inserted through a vacuum lock mechanism.

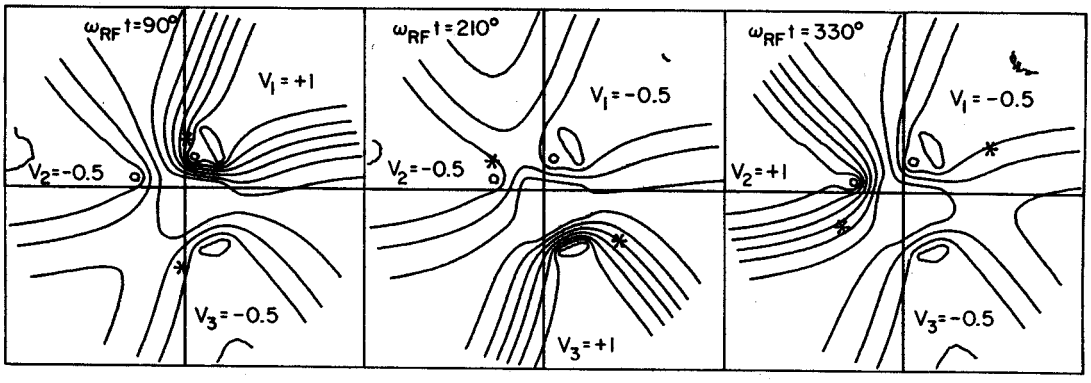

Fig. 6. Equipotentials for the h=2 central region at three different times. This figure shows the actual time dependent potential distribution for the h=2 electrode configuration of Fig. 5 as it would appear at three different t values. The asterisks indicate the simultaneous positions of the ions in the central ray orbit of Fig. 5. For h=2, there are two ion bunches per turn. Note that the electric field in the gap is higher when the ions exit the dees than when they enter. This indicates that the ions are injected with a positive phase (i.e. "late"), which is done purposely in order to increase the vertical electric focusing. In contrast, an ion with zero phase would cross the dee center at zero voltage and see equal electric fields when entering and leaving the dee.

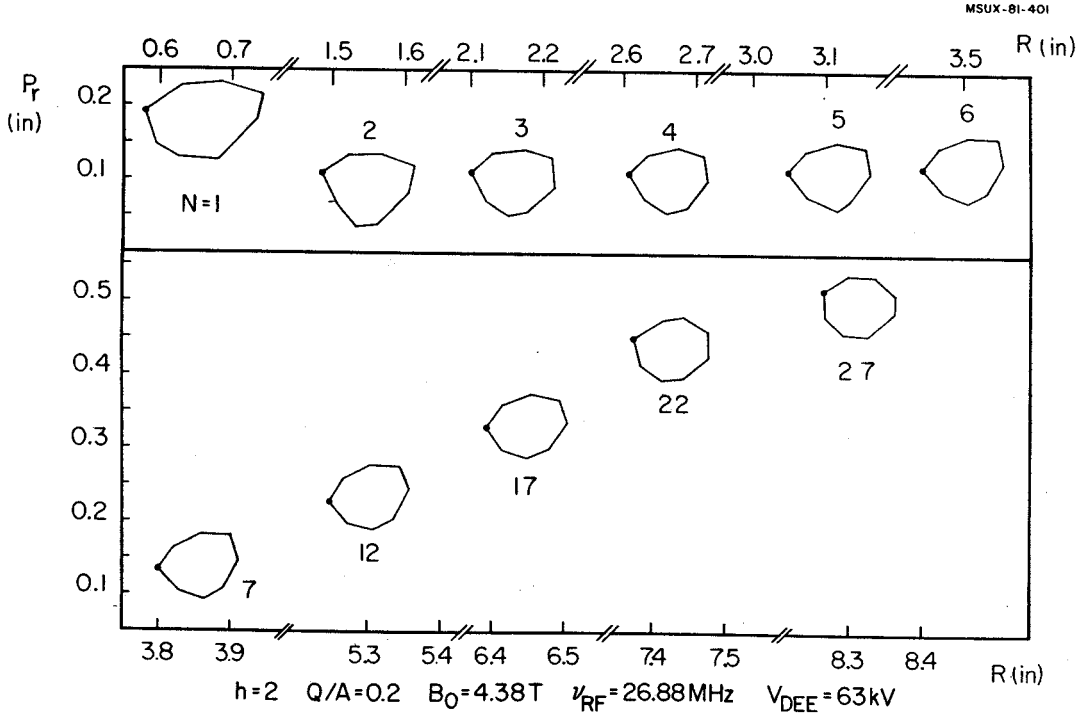

Fig. 7. Radial phase space, h=2. In addition to the central ray orbit, we calculated eight displaced rays with initial conditions defining a circular area in the (r,p_r) phase space. These rays were traced backward starting near r=10 inch, with the same energy and average phase as the central ray. We show here the (r,p_r) motion of the eight rays, once per turn at $\theta=60°$.

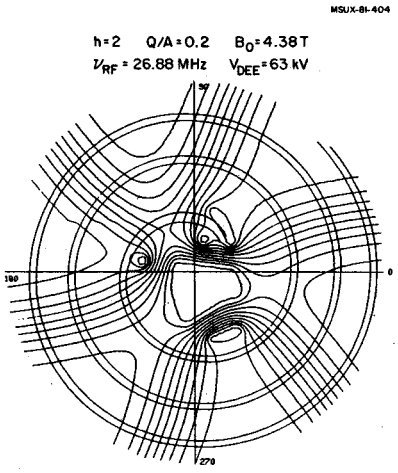

Fig. 8. Beam envelope in radial space, h=2. Beam envelope in the median plane for h=2 as determined from the eight rays described in Fig. 7.

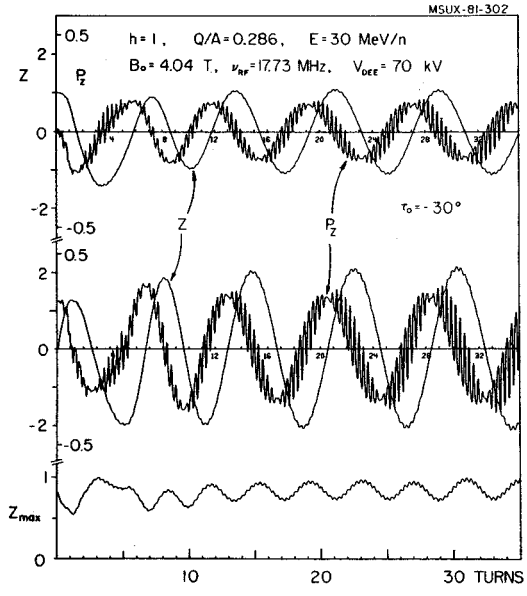

Fig. 9. Vertical motion and resultant beam envelope. The top and center curves show the z and p_z variations for two independent solutions representing the vertical motion for the h=1 central ray orbit shown in Fig. 3 and Fig. 4 (middle curve). Electric focusing dominates on the first few turns, and its importance relative to magnetic focusing declines steadily thereafter. As can be seen, the overall period of the vertical oscillations varies from about seven to nine turns, and superimposed on this variation is the thrice per turn oscillation due first to the gap crossings, and later to the magnet sectors. The bottom curve shows the corresponding variation of the beam envelope (normalized to a maximum of 1.0) which would be obtained for a beam matching the maximum vertical acceptance.

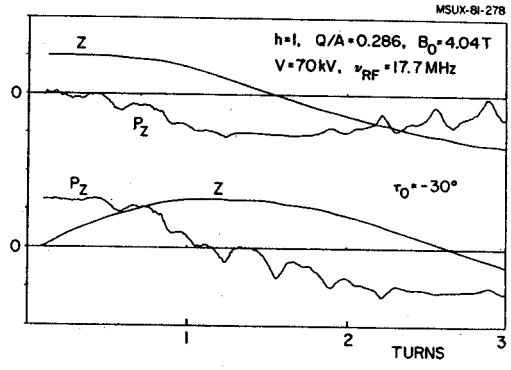

Fig. 10. Vertical motion. Expanded view of the top and center curves of Fig. 9 for the first three turns.

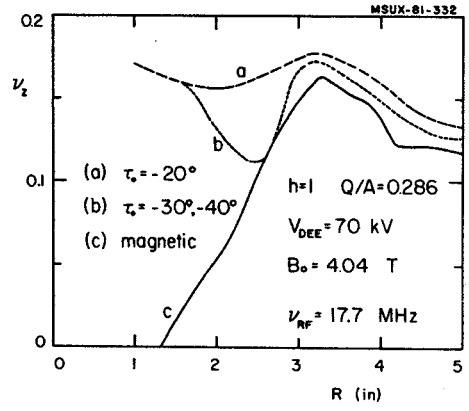

Fig. 11. Vertical focusing frequency versus radius for h=1 (530 turns) orbits. This figure presents estimates of ν_z vs. r derived from graphs similar to those at top and center of Fig. 9 for the three h=1 orbits whose phase variations are shown in Fig. 4. The solid curve gives the magnetic focusing values obtained from the equilibrium orbit code. Note the substantial improvements in ν_z produced by electric focusing at the lowest r values.

From the wavelength of oscillations in the z-motion curves like those shown in Figs. 9 and 10, we can estimate the vertical focusing frequency ν_z and compare the results to the corresponding magnetic values. An example of this comparison is shown in Fig. 11 and the importance of electric focusing at small radii is quite obvious.

Nickel Plating the K-500 Cryostat

H. Hilbert, J. Yurkon, D. Poe, D. Capelli, R. Zarobinski and T. Dennany

The vacuum requirement for the operation of the heavy ion beams requires that materials with low outgassing rates be used in the vacuum chamber of the K-500 cyclotron. Because clean non-oxidized steel has an outgassing rate 20 times that of nickel plated steel plus plating would also inhibit the corrosion of the steel it was decided to nickel plate the inside surface area of the cryostat.

Plating the inside of the cryostat presented several problems. First, its size and delicate nature ruled out the method most often used in industry (where parts to be plated are completely immersed during the cleaning process in a 140°F alkaline solution followed by a 140°F acid pickle before its final immersion in a plating bath.) Because of its size, thermal-mass and danger to its critical support structures the above process was ruled out.

After a series of small scale tests it was found that if the steel to be plated was very clean and free of oxide it is possible to nickel plate at room temperature using commercial solutions available from any plating shop.

Brush plating after a cleaning procedure of sand blasting followed by the removal of oxidation just prior to plating by wiping the steel surface with a solution of 15% HCl. Before any cleaning took place all the delicate parts of the cryostat such as bellows, stainless steel tubing and critical welds were covered with plastic and taped.

It is common in immersion type nickel plating to operate with current densities of 40-50 amp ft^2. Therefore a deposit of .00025 inch of nickel on an area of1 ft^2 requires 4.75 amp-hours at 100% plating efficiency.

With a total area to be plated of 55 ft^2 it was decided to build a large anode for open areas and a small one for the confined areas. The small anode was made from standard one inch diameter x six inch nickel anode rod. One end was tapped to accomodate a handle fashioned from 1/4" stainless steel as shown in photograph #1. The nickel rod was covered with rayon wool, held in place with a sock, to prevent direct contact of the anode with the surface to be plated, and also to act as a mop for the electrolyte solution. This design presented a surface area of about 6 square inches. Normal current densities for nickel plating baths are around 40-50 amps/sq. ft. The total integrated current to produce a plate .00025 inches of nickel over 1 sq. ft surface is 9.5 amp-hours. Therefore, this anode requires approximately 4.7 hours to plate 1 square foot.

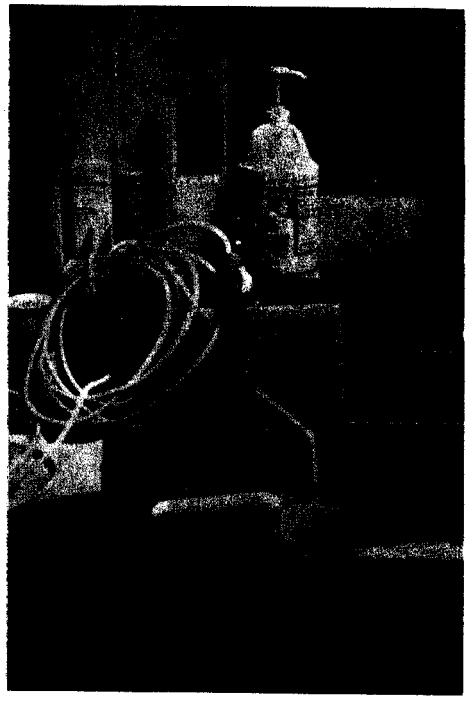

In practice we were able to plate faster than this since the electrolyte flowed out over the surface reducing the current density and permitting a high current of about 5 amps. This higher current then reduces the time to about 2 hr/sq. ft.

The large anode was made from 3 eliptical bars of nickel of dimensions 3.5" x 3" x 1" tied together with nickel straps to form an electrode of approximate dimensions 8" x 12". This anode was covered with rayon wool held in place with a synthetic cloth cover. Cotton is inadequate, as it is attacked by the acids used. Plating solution was supplied to this anode by the use of a small pump. This brush was operated at 50 amps, thus requiring 12 minutes per square foot to deposit a nickel plating of .00025 inches thick. Due to its weight of 25 lbs, and the time required to plate a given surface, it was necessary to counter-weight the large anode.

Plating Procedure

The area to be plated was chosen to be large enough to require 2 hours time. This was not so long as to be tiring to personnel but long enough to provide an acceptable set up time to plating time ratio. All areas except the one to be plated were protected with visqueen and duct tape to protect the clean surface left by sand blasting. The area to be plated was then wiped with a 15% hydrochloric acid solution.

Plating was immediately started to prevent further oxidation. The current through the anode was integrated to provide information on the thickness of nickel deposited. Simply recording the time is inadequate since absolute current control cannot be maintained. Plating personnel were rotated during this 2 hour period so as not to interupt the plating process. After the plating was completed the surface was rinsed with a baking soda solution to neutralize any acid salt residue and then carefully dried.

Problem Encountered

Careful current control had to be maintained since excessive current produced burned deposits which interferred with subsequent plating.

Areas that had received insufficient plating were replated. Replating however was difficult since the nickel oxides formed during exposure to air are not easily removed prior to replating (this caused plated surfaces to peel at a later time). Careful cleaning reduced but did not eliminate this problem. The process of flowing plating solution on to the anode, gassing of the solution during electrolysis, and splashing of solution returning to the resevoir produced a vapor which collected on all unprotected surfaces. Because this vapor is corrosize to nickel it was important to protect the areas already plated.

After the problems encountered plating a completed cryostat we hope to plate the next one before the critical components are installed.

Coupling of Radial and Longitudinal Motion in Cyclotrons

M.M. Gordon and Felix Marti

For most cyclic accelerators, the fractional energy gain per turn is so small that the acceleration process can be accurately described as "adiabatic". However, this is generally not true for cyclotrons since they accelerate ions for relatively small numbers of turns starting, in most cases, from nearly zero energy.

As a result, the median plane motion in cyclotrons is accompanied by exceptionally strong coupling of the acceleration process and the radial oscillations within the beam. The strength of this coupling varies inversely with turn number so that its effects are most pronounced in the central region. In many cases, however, these effects remain significant throughout the cyclotron. This is especially true when the rf system operates on a high harmonic h of the orbital frequency since the coupling strength is also proportional to h.

Recently, Schulte and Hagedoorn[1] have published the first comprehensive analysis of these coupling effects. Unfortunately, their analysis is based on a non-relativistic Hamiltonian and formulated in cartesian coordinates, which restricts the scope and accuracy of their results.

Nevertheless, their work clearly outlines at least two important aspects of the coupling process which deserve further investigation. One of these concerns the proper definition of the phase ϕ for particles executing radial oscillations, and the other concerns a phase dependent shift in ν_r produced by the acceleration process which can, in certain cases, lead to radial instability.

Regarding the phase definition, there is the average phase ϕ which determines the energy gained by a group of particles when averaged over many gap crossings, and then there is the "local" phase ($\omega_{rf}t$) which specifies the time at which different members of the group cross a particular gap. The problem of correlating these phases was solved, at least for a nearly uniform magnetic field, by Schulte and Hagedoorn who identified ϕ with a "central position" phase.

For the more general case, we have found that the definition of ϕ should be revised so as to make it a constant of the motion for a group of monoenergetic particles executing radial oscillations. For example, when the equilibrium orbit is circular, we obtain the relation:

$$\phi = \omega_{rf}t - h\theta + hp_x/p\nu_r^2.$$

In this case, ions having the same ϕ value will generally start out with different values of the local phase, but will finally end up with very nearly the same energy gain. Thus, this revision serves to maintain the energy homogeneity of the group.

An investigation of the second effect noted above, namely, the phase dependent shift in ν_r produced by the acceleration process, convinces us that it should be called "radial electric focusing" since we find a striking similarity between the results obtained for this effect and those obtained in a previous paper dealing with vertical electric focusing.[2] This similarity even extends to the presence of the same alternating gradient focusing in both cases for certain dee geometries.

Indeed, we find here a kind of "complementarity" relationship between the radial and vertical electric focusing which resembles, at least on the surface, the one discovered by Dutto and Craddock[3] for a completely different aspect of electric focusing. That is, when acceleration conditions are modified so as to increase the vertical focusing, then they will simultaneously decrease the radial focusing by a comparable amount.

This complementarity is particularly surprising since the nature of the focusing force for the radial oscillations is basically so different from that for the vertical oscillations. In the radial case, the force resembles an inertial force since it arises from the accelerated motion of the "reference frame". That is, the radial oscillations are performed about an equilibrium orbit which shifts outward in position at each gap crossing.

A paper on this work has recently been completed and submitted for publication in Particle Accelerators. In this paper, we evaluate the change in ν_r for a fairly general dee geometry, and then show that for certain cyclotrons, namely those having one or two dees, the radial oscillations may become unstable near $\nu_r = 1$ through a mechanism similar to the production of a stop-band at a half-integral resonance. These results are then applied to a number of cyclotrons including one at Indiana and the TRIUMF machine.

---

1. W.M. Schulte and H.L. Hagedoorn, Nucl. Instrum. Methods, 171, 409 (1980).
2. M.M. Gordon and F. Marti, Particle Accelerators, 11, 161 (1980).
3. G. Dutto and M.K. Craddock, Proc. 7th Int. Conf. on Cyclotrons (1975), p. 271.

Neutron Shielding for Phase II Operation

J. Naryanaswami, J. Duffy, Z. Koenig, R. Ronningen and E. Kashy

The radiation shielding for phase II consists of a combination of the concrete shield walls shown in Fig. 1 and of local shielding at the various positions where beam is stopped. These are mainly at the Faraday cups at the end of each beam line, but include beam defining slits and beam stops at certain locations in the beam transport system. The material for the local shielding is iron and the required thicknesses at the various points are being calculated so that the radiation level at any point outside the shield walls will remain below 2.5 mr per hour. By achieving this dose rate we expect that the integrated exposure of radiation personel will be far below the limits of 5 rems/per year.

sum of neutron emission from projectile fragmentation and of evaporation from a source moving at half the beam velocity. A comparison of the calculated spectra with measurements[1] of neutron yields at 0^{o} and 45^{o} for 710 MeV alpha particles stopping in water is shown in Figs. 2 and 3. The resulting spectra of neutron before the local shielding is included is shown in Fig. 4, for the location marked by "*" in Fig. 1 and for the beam stopping at the 120" scattering chamber. The typical "hardening" of the spectrum is clearly seen.

Figure 5 shows the result of adding local shielding consisting of 150 cm of iron at 0^{o}. A report giving details of these calculations

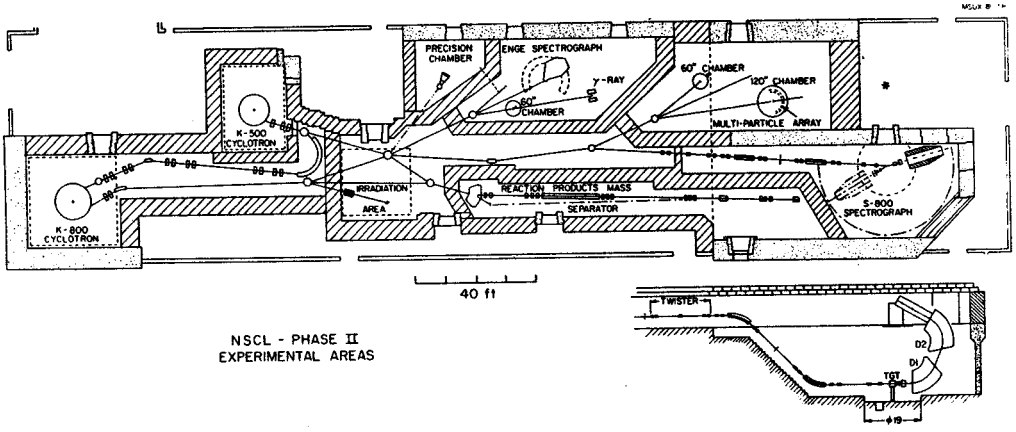

Fig. 1

In addition to reducing the neutron flux outside the vaults, the local shieldings greatly reduce the irradiation of the air inside the vaults which is mainly caused by the (n,2n) reaction on ^{16}O, ^{14}N and ^{12}C. The skyshine effect is also minimized by the local shielding provided.

The design of the beam dumps is based upon neutron yields expected from the various beams to be used in our facility. Experimentalists were interviewed to learn the types of beams they expect to use, their intensities, and the frequency of usage of the various beams. A set of 9 typical beams was selected in order to arrive at the expected intergrated radiation dose.

A relatively simple form of $\frac{d^2\sigma}{d\Omega dE}(\theta)$ for the emitted neutrons was arrived at in consultation with Prof. Bertsch and Prof. Scott so that the neutron production by heavy ion beams could be predicted. These cross sections were then intergrated over the ion range in the stopping medium (i.e. water in the faraday cup) resulting in neutron spectra at various angles with respect to the beam. The form of $\frac{d^2\sigma}{d\Omega dE}(\theta)$ is taken as the

MSUX-81-406

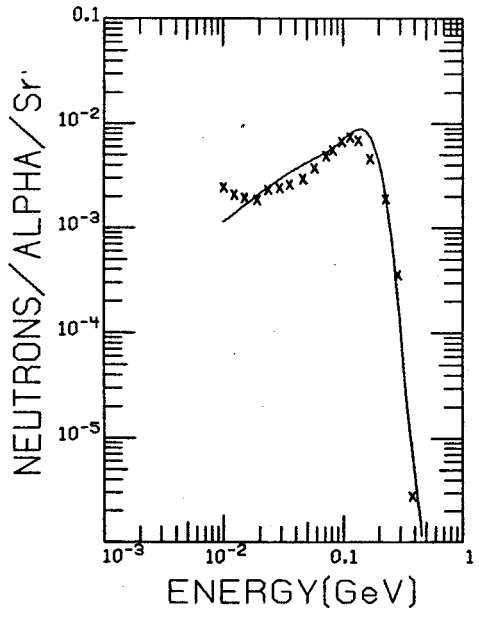

Fig. 2

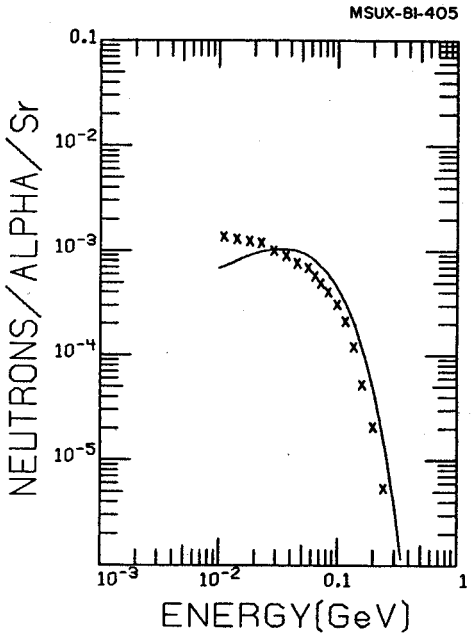

Fig. 3.

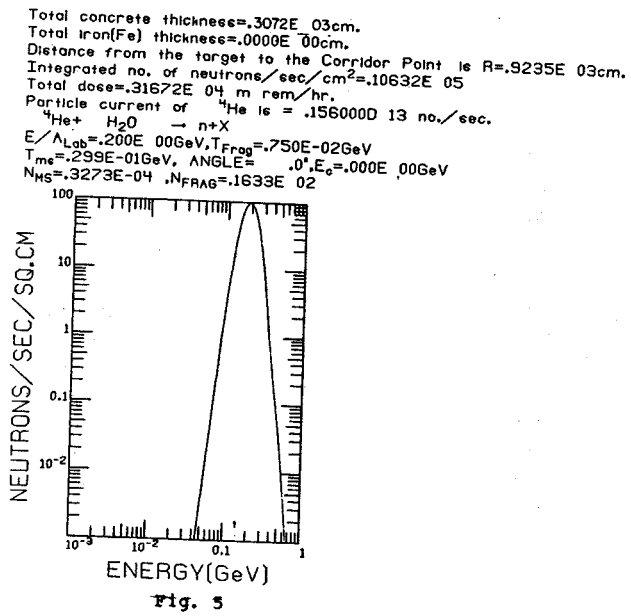

Fig. 5

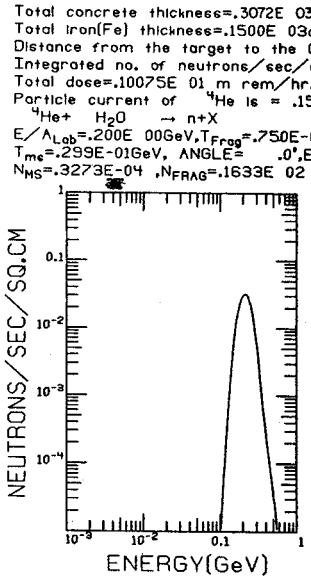

Fig. 4

as well as integrated radiation dose predictions for a whole year's operation is being prepared.

---

1. R.A. Cecil, B.D. Anderson, A.R. Baldwin, R. Madey, A. Galonsky, P. Miller, L. Young and F.M. Waterman, Phys. Rev. C21 2471 (1980).